A numerical parameter study of the beam-target interaction performed at KALIF

Abstract

The Karlsruhe Target Code **KATACO** is used to simulate beam-target interaction experiments performed with the Karlsruhe Light Ion Facility **KALIF**. This report summarizes the main results of a numerical parameter study with different assumptions about the maximum power density of the **KALIF** diodes, the beam angle and energy distribution and the beam power rising and decreasing time. A discussion of the role of radiative transfer and two-dimensional effects is included. The calculations show that more detailed information is needed about the beam parameters at the target during individual **KALIF** shots for a better interpretation of single experiments. A simultaneous measurement of target velocities *and* temperatures of the generated ablation plasma is desirable. The two-dimensional simulations suggest the possibility to deduce information about the spatial beam profile of **KALIF** from spatially resolved measurements of the target velocity.

Eine numerische Parameterstudie der Strahl-Target Wechselwirkung am KALIF

Zusammenfassung

Mit dem Karlsruher Target Code **KATACO** werden Strahl-Target Experimente simuliert, die an dem Leichtionenbeschleuniger **KALIF** durchgeführt werden. Der vorliegende Bericht faßt die wesentlichen Ergebnisse einer numerischen Parameterstudie zusammen, in der unterschiedliche Annahmen über die maximale Leistungsdichte der **KALIF**-Dioden, die Winkel- und Energieverteilung der Protonen sowie die Anstiegs- und Abfallszeit der Strahlleistung untersucht wurden. Ferner wird der Einfluß von Strahlungstransportprozessen und zweidimensionalen Effekten diskutiert. Die Rechnungen zeigen, daß für die weitere Analyse einzelner Experimente detailliertere Informationen über die Strahlparameter am Target während der betreffenden **KALIF**-Schüsse notwendig sind. Die gleichzeitige Messung von Targetgeschwindigkeiten *und* Temperaturen des erzeugten Ablationsplasmas sollte angestrebt werden. Die zweidimensionalen Simulationen zeigen die Möglichkeit auf, anhand von räumlich aufgelösten Messungen der Targetgeschwindigkeiten Informationen über das räumliche Strahlprofil des **KALIF** zu gewinnen.

1 Introduction

The Karlsruhe Target Code (**KATACO**) simulates the 1-dimensional hydrodynamic, thermodynamic and radiative behaviour of a plasma irradiated by intense ion beams and is extensively used to study beam-target interaction experiments performed with the Karlsruhe Light Ion Facility (**KALIF**). The plasma is described by four main variables ρ, u, T_i and T_e, representing the mass density, mass velocity, ion and electron temperature as functions of a single space coordinate and time (single-fluid two-temperature approximation). The governing equations expressed in a moving Lagrangian coordinate system are:

- The Euler equation of motion

$$\rho \frac{du}{dt} = -\nabla (p_\mathrm{i} + p_\mathrm{e}), \tag{1}$$

  where p_i and p_e are the pressures of the ion and electron gas.

- Two equations for the temperature of the electronic and ionic subsystem in the form of the time derivative of the first thermodynamic law

$$(C_V)_\mathrm{i} \frac{dT_\mathrm{i}}{dt} + (B_T)_\mathrm{i} \frac{d\rho}{dt} + p_\mathrm{i} \frac{dV}{dt} = H_\mathrm{i} - K + Y_\mathrm{i} + Q \tag{2}$$

$$(C_V)_\mathrm{e} \frac{dT_\mathrm{e}}{dt} + (B_T)_\mathrm{e} \frac{d\rho}{dt} + p_\mathrm{e} \frac{dV}{dt} = H_\mathrm{e} + K + Y_\mathrm{e} + X + E_\mathrm{r}\ (+J) \tag{3}$$

  with

$$(C_V)_\mathrm{i,e} = \left(\frac{\partial U_\mathrm{i,e}}{\partial T_\mathrm{i,e}} \right)_\rho \tag{4}$$

$$(B_T)_\mathrm{i,e} = \left(\frac{\partial U_\mathrm{i,e}}{\partial \rho} \right)_{T_\mathrm{i,e}} \tag{5}$$

  where
  $U = U(r,T)$ represents the internal energies per unit mass,
  $H = H(r,T) = \nabla \cdot (\kappa \nabla T)$ is the flow of heat due to thermal conduction,
  $K = K(r,T)$ is the rate of energy exchange between electrons and ions,
  $Y = Y(r,T)$ is the rate of thermonuclear energy release from fusion processes,
  $X = X(r,T)$ is the rate of (ion) beam energy absorption,
  $Q = Q(r,T)$ is the rate of viscous shock heating,
  $E_\mathrm{r} = E_\mathrm{r}(r,T)$ is the rate of radiative energy exchange between photons and the plasma.

  In cases where radiation transport is not calculated one may wish to include at least the Bremsstrahlung losses. In this case E_r is replaced by the rate of Bremsstrahlung emission $J = J(r,T)$.

- Two independent equations of state for ions and electrons

$$p_\mathrm{i} = p_\mathrm{i}(\rho, T_\mathrm{i}) \tag{6}$$

$$U_\mathrm{i} = U_\mathrm{i}(\rho, T_\mathrm{i}) \tag{7}$$

$$p_\mathrm{e} = p_\mathrm{e}(\rho, T_\mathrm{e}) \tag{8}$$

$$U_\mathrm{e} = U_\mathrm{e}(\rho, T_\mathrm{e}) \tag{9}$$

- Multiangle, multigroup radiation transport in planar geometry, coupling the equation for the electron temperature (3) with the difference between emitted and absorbed radiative energy by summing the contributions over all considered frequency groups g,

$$E_\mathrm{r} = c \sum_{g=1}^{G} \left(\sigma_{\mathrm{e},g}\, b_g\, a T_\mathrm{e}^4 - \sigma_{\mathrm{a},g}\, E_{\mathrm{r},g} \right) \ . \tag{10}$$

Here, the radiation energy density $E_{\mathrm{r},g}$ in the frequency group g is given by the transport equation

$$\frac{\partial E_{\mathrm{r},g}(\vec{\Omega})}{\partial t} + c\ \vec{\Omega}\cdot\nabla E_{\mathrm{r},g}(\vec{\Omega}) = c\left\{\sigma_{\mathrm{e},g}\, b_g\, a T_{\mathrm{e}}^4 \frac{d\vec{\Omega}}{4\pi} - \sigma_{\mathrm{a},g}\, E_{\mathrm{r},g}(\vec{\Omega})\right\}\ , \tag{11}$$

where
c is the speed of light,
$\sigma_{\mathrm{e},g}$ is the radiative emission coefficient in frequency group g,
$\sigma_{\mathrm{a},g}$ is the radiative absorption coefficient in frequency group g,
$\vec{\Omega}$ is the space angle direction of photons,
$d\vec{\Omega}$ is the solid angle element in direction $\vec{\Omega}$,
and a is the radiation constant connected to the Stefan Boltzmann constant σ_{SB} by

$$a = \frac{8\,\pi^5 k^4}{15\,h^3 c^3} = \frac{4\,\sigma_{\mathrm{SB}}}{c}\ . \tag{12}$$

In each frequency group g the fraction of the radiative source is $b_g a T_{\mathrm{e}}^4$ and the corresponding radiation energy density is $E_{\mathrm{r},g}$. The frequency group fractions b_g arise from the following weighting of Planck functions in the frequency intervalls (ν_{g-1}, ν_g)

$$b_g(\nu_g, T_{\mathrm{e}}) = \frac{\int_{\nu_{g-1}}^{\nu_g} B(\nu)\, d\nu}{\int_0^{\infty} B(\nu)\, d\nu} = \frac{\int_{\nu_{g-1}}^{\nu_g} \dfrac{2h\nu^3}{c^2\left(\exp(\frac{h\nu}{kT_{\mathrm{e}}}) - 1\right)}\, d\,\nu}{\dfrac{acT_{\mathrm{e}}^4}{4\pi}}\ , \tag{13}$$

with

$$\sum_{g=1}^{G} b_g = 1\ . \tag{14}$$

In this way the continuous frequency range is divided into frequency groups with the assumption of frequency averaged quantities $E_{\mathrm{r},g}$, $\sigma_{\mathrm{e},g}\ \sigma_{\mathrm{a},g}$ and b_g in each group (multigroup approach).

By default, the time dependent radiation transfer equations in **KATACO** are solved by the radiation package MULRAD (Goel et al. 1993). Here we use instead the time independent diffusion aproximation of MULTI which has recently been tested and implemented in **KATACO** (Gupta et al. 1997a,b).

This report summarizes the main results of a numerical parameter study of beam-target interaction experiments performed at **KALIF**. Recently, Goel & Vorobiev (1996) have demonstrated that the equation of state is of crucial importance for modeling the acceleration of solid targets irradiated by **KALIF** proton beams. The failure to reproduce the measured velocity history of the accelerated targets with e.g. the equation of state (EOS) given by Bushmann et al. (1989) or by the SESAME tables lead to the development of a semiempirical EOS in a generalized Mie-Grüneisen form by assuming that the Grüneisen parameter not only depends on the density but also on the energy of matter. However, this semiempirical EOS is thermodynamically incomplete since it only provides the quantities necessary to compute pure hydrodynamics based e.g. on a Godunov-type solution formalism, i.e. $p = p(\rho, u)$, $u = u(\rho, p)$ and $c_{\mathrm{s}} = c_{\mathrm{s}}(\rho, p, u)$, where ρ, p, u and c_{s} are the density, pressure, internal energy and sound velocity, respectively. Especially, it does not explicitly contain the temperature nor temperature derivatives which are required in **KATACO** (see eqs. (2)-(5)), with the result that it cannot be used here. Therefore, we began a project for the development of a thermodynamically *complete* EOS which not only describes the **KALIF** but also all other shock wave experiments. The recent status of this EOS is what we call the

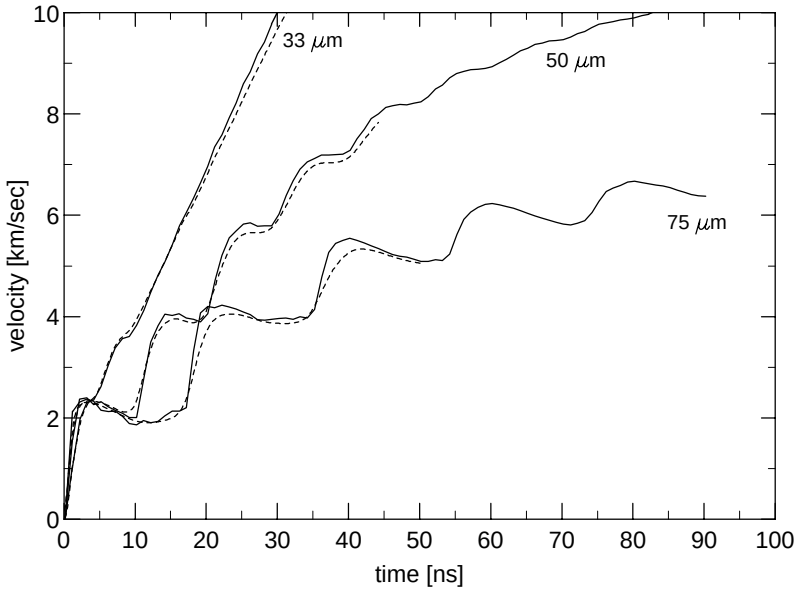

Figure 1: Computed evolution of the velocities of 33, 50 and 75 μ thick aluminum foils after irradiation with the **KALIF** B_Θ-diode. Solid lines: results of the code **KATACO**; dashed: 2nd order Godunov scheme according to Goel & Vorobiev (1996). All calculations are based on the unified tabulated EOS (see text).

unified tabulated EOS, a combination of the Bushmann EOS developed from shock compression data of solid matter, and a model based on chemical potentials for low densities and high temperatures. Fig. 1 shows a comparison of target velocities after the impact of the **KALIF** proton beam, once computed with **KATACO** and once with a 2nd order Godunov scheme (Goel & Vorobiev 1996) both using this unified tabulated EOS. Although the numerical schemes are completely different (see discussion above) and have been developed independently, they show satisfactory agreement of the results.

Accompanied with the development of a thermodynamically complete EOS one has to check, which of the physical processes in the **KALIF** diodes (e.g. diode instabilities) influence the beam-target interaction and to which extent. Also, the diode and beam characteristics are subject to experimental uncertainties, most of which are connected to the reproducibility of the characteristics of **KALIF**. Finally, for the development of an EOS it is important to know the processes in the target like thermal conduction or radiative transfer which could influence the observed quantities.

This report summarizes the main results of a numerical parameter study adressed to answer some of the above mentioned questions. It is not complete in that not all of the effects and their combinations have been checked for both currently used **KALIF** diodes (B_Θ and $B_{\rm appl}$) and for computational reasons not all of the models have been worked out including full radiative transfer. The studied effects to be discussed in the next sections are:

- models without radiative transfer
  - the effect of a homogeneous beam angle distribution (B_Θ)
  - changes in the diode current with beam angle and time ($B_{\rm appl}$)
  - the effect of a proton energy distribution (B_Θ)
  - the influence of the maximum power density (B_Θ and $B_{\rm appl}$)
  - two-dimensional effects (B_Θ)
- models including radiative transfer
  - the influence of Bremsstrahlung and radiative transfer (B_Θ and $B_{\rm appl}$)
  - the influence of the beam rising and decreasing time ($B_{\rm appl}$)

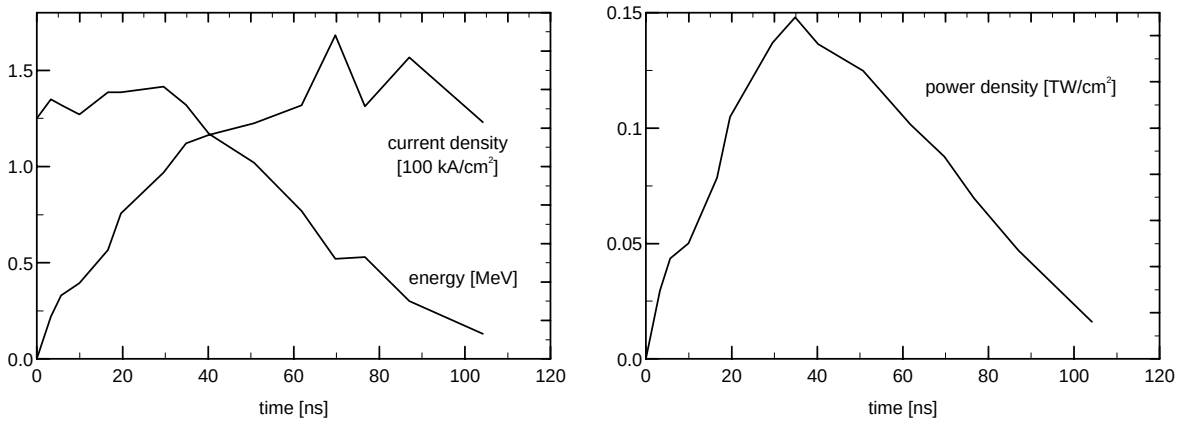

Figure 2: Average current density and energy (left) and power density (right) of the B_Θ proton beam on target.

2 The effect of a homogeneous beam angle distribution (B_Θ)

Both, the B_Θ- and the $B_{\rm appl}$-diode are designed for ballistic focusing of the ion beam. For the B_Θ-diode the angle of incidence on the target surface is between 20° and 40° (angle between the beam and the target normal). It has been found that the beam of the B_Θ-diode is neither homogeneous in radial nor in azimuthal direction. However, in this section, we assume that the beam is homogeneous within the geometrically limiting beam angles of 20° and 40°. Beam inhomogenities like patches could in principle be simulated in 1D-calculations by statistically varying the power density with time, however, the consideration of statistical processes is beyond the scope of the present paper. The effect of a *systematic* radial development of a diode current with time is demonstrated exemplarily for the $B_{\rm appl}$-diode in the next section. The average beam parameters of the B_Θ-diode on target as determined experimentally by Hoppé et al. (1995) are shown in Fig. 2.

With the beam characteristics shown in Fig. 2, computations have been performed for the following angles of incidence θ: single-beam calculations with θ = 20°, 30°, 40°, and a multiple-beam calculation with four beams coming from θ = 22.5°, 27.5°, 32.5° and 37.5°. In the latter case it has been assumed that each of the four beams carries one fourth of the total current density so that the total power density is kept as shown in Fig. 2. This case well approximates a homogeneous beam angle distribution.

Results of the computations are shown in Fig. 3 in terms of the target back surface velocity for the irradiation of a 75 μm thick aluminum target. The cases for $\theta = 20°$ and $\theta = 40°$ simulate the most extreme conditions that the beam comes either from the smallest or largest geometrically possible direction, and the differences in the targets back surface velocities are easily understood: Since for a given proton beam energy the proton range depends on $\cos\theta$, the remaining target thickness is larger for a larger angle of incidence. Therefore, the reverberation time of the shock wave induced by the proton beam becomes larger with increasing θ (longer velocity steps), and the final velocity becomes smaller because more mass has to be accelerated by the ablation plasma. The simulation for $\theta = 30°$ also shown as a solid line in Fig. 3 simulates the (as well extreme) case of a **KALIF** beam coming completely from the geometrically centered direction. However, a comparison with the simulation of a homogeneous beam angle distribution (dashed in Fig. 3) shows that the differences between these two cases are only small. Mainly, the velocity steps are slightly smoothed due to a less steep density gradient at the plasma-solid interface. A distribution of the proton depth due to a large number of impact angles results in a smoothing of the Bragg peak in the energy deposition (Fig. 4). Consequently, the density gradient at the plasma-solid interface becomes less steep and shock reflections (which result in the velocity steps seen in Fig. 3) take place over a larger region.

These simulations show that the angle of incidence is an important parameter which determines the target velocity after impact for a given target thickness ($\theta = 0$ would give a maximum acceleration). However, a simulation with a homogeneous distribution of impact angles does not differ significantly from a calculation with a single beam of average angle.

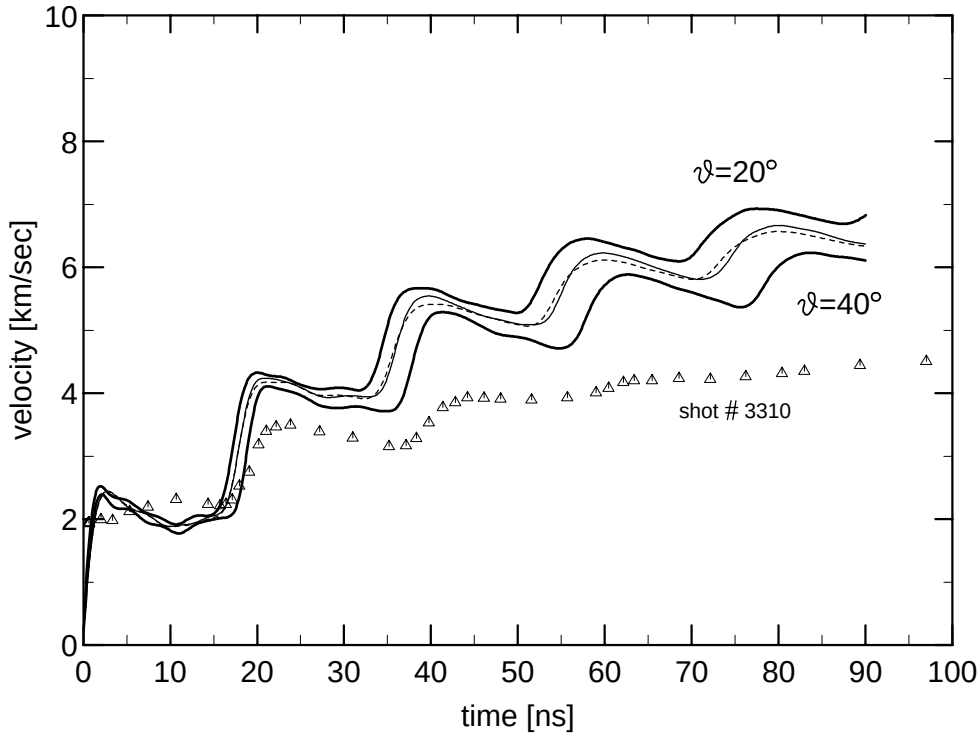

Figure 3: Simulated back surface velocities of a 75 μm thick aluminum foil after impact of the B_Θ proton beam at different angles of incidence θ. Thick lines show calculations for single beams with $\theta = 20^\circ$ and 40°. The thin solid line shows a simulation for a single beam with $\theta = 30^\circ$, the dashed line is a simulation for a homogeneous beam angle distribution (see text).

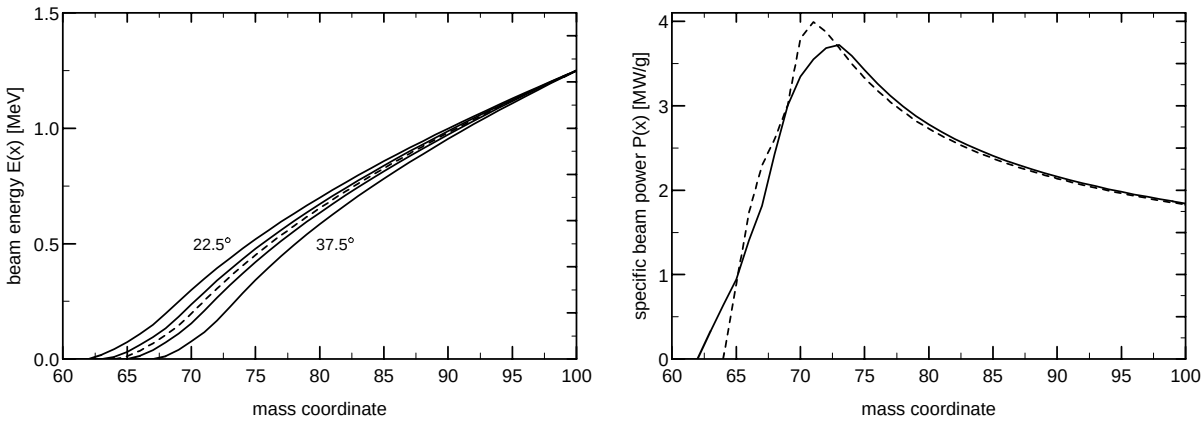

Figure 4: left: Beam energy as a function of the mass coordinate for different angles of incidence (θ = 22.5°, 27.5°, 32.5°, 37.5°) at $t = 0$ (solid lines). The beam enters the target surface at mass coordinate 100 from the right. The dashed curve shows the beam energy for the single-beam computation with $\theta = 30^\circ$. right: total specific beam power as a function of the mass coordinate for the homogeneous beam angle distribution (four beams, solid line) and for the single-beam computation with $\theta = 30^\circ$ (dashed).

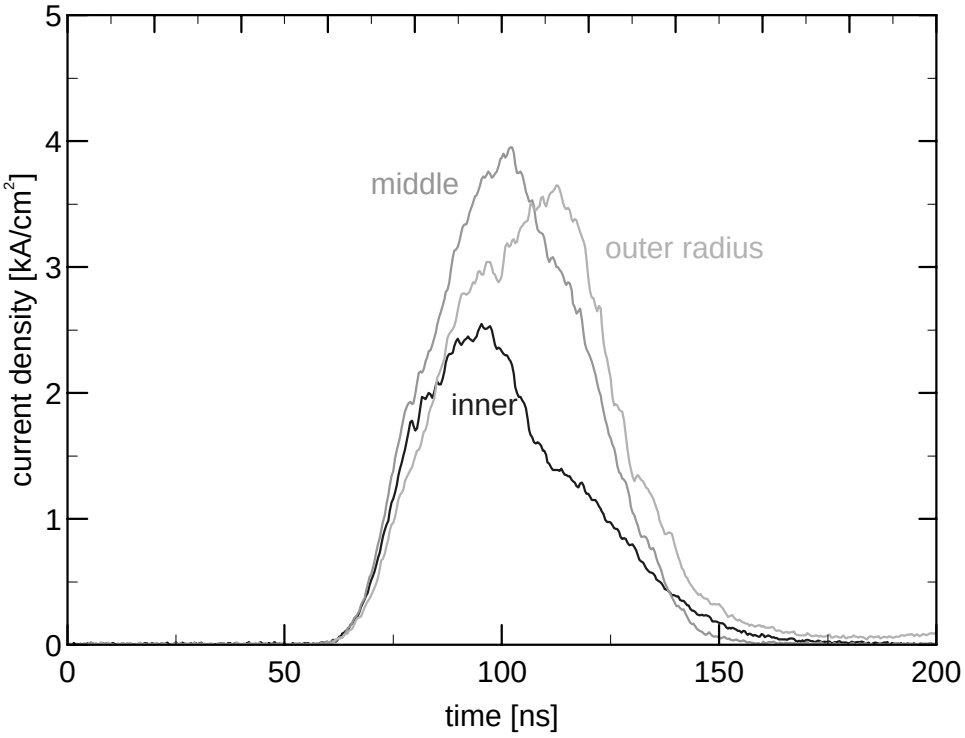

Figure 5: Average current densities measured by Faraday cups placed at radii of 67.66 (inner), 74.92 (middle) and 80.22 mm (outer) inside the diode gap (see text). Note the time shift of the maxima between the inner and outer radius.

3 Changes in the diode current with beam angle and time (B_{appl})

For the B_{appl}-diode the geometrically possible angles of incidence on the target are between 30° and 42.5°. For this diode it has been found that the diode current developes radially outwards with time, i.e. the angle of incidence for an average beam on the target may change with time. This has been discovered by placing Faraday cups at different radial and azimuthal positions inside the diode gap. Altogether, 12 Faraday cups arranged in three groups have been placed at diode radii of 67.66, 74.92 and 80.22 mm. These diode radii, which we will call inner, middle and outer radius in the following, correspond to angles of incidence of 35.7°, 37.9° and 39.9° at the target. Averages have been taken over the four current densities at each radius and over ten diode shots, thereby averaging over azimuthal as well as shot-to-shot variations. The resultant average current densities as a function of time are shown in Fig. 5. Clearly, there is a time shift between the maxima of the signals of more than 20 ns between the inner and outer diode radius.

Unfortunately, it is not straight forward to compare the current *densities* measured by the Faraday cups with electrically measured *currents*, or even to derive proton current densities on target. For simplicity we assume for the following calculations that each group of Faraday cups at the three different radii covers $1/3 \approx 42\,\mathrm{cm}^2$ of the total diode emission area.[1] The resultant *currents* derived from the Faraday cups are compared to the electrically measured signals of the diode in Fig. 6. This figure shows the well known fact that the electrically measured current almost perfectly agrees with the sum of the

[1]The Faraday cups have a small entrance hole and it is difficult to determine the true part of the diode emission area seen by each of these cups. Taking into account their true radial positions, assuming that the areas they see do not overlap and treating the diode emission surface as a segment of a cone gives areas of 63, 28 and $40\,\mathrm{cm}^2$ covered by the inner, middle and outer group of Faraday cups, respectively. The difference to the assumed $42\,\mathrm{cm}^2$ however is not very important for the following simulations.

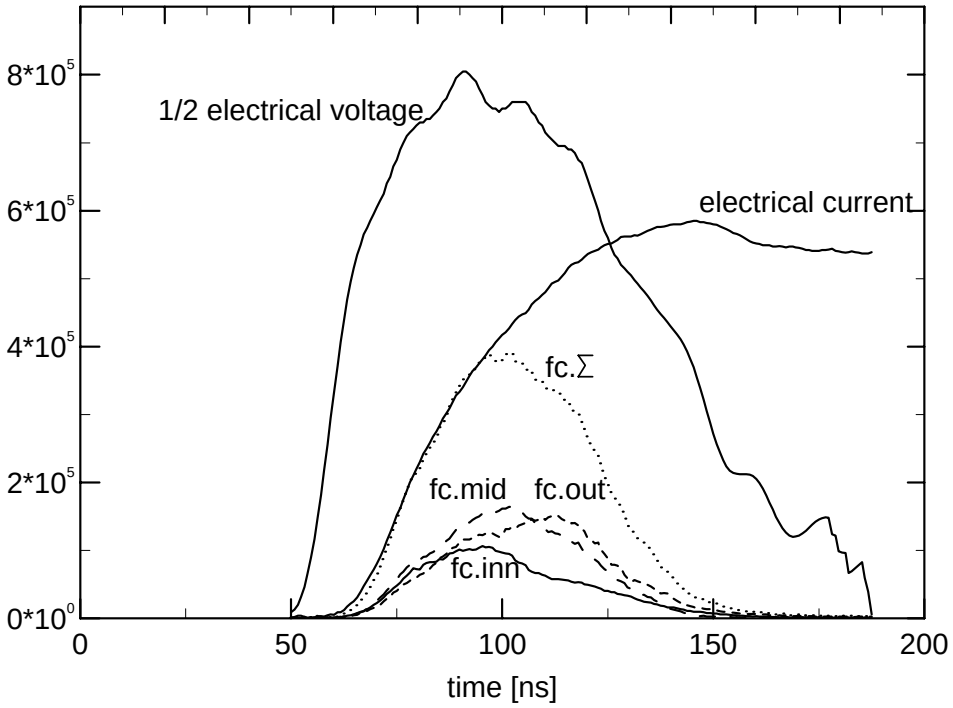

Figure 6: Measured electrical voltage and current of the B_{appl}-diode as well as Faraday currents (see text) as a function of time. The voltage is in Volts, all currents are given in Ampéres.

Faraday currents until the growing of a parallel load during diode operation (Bluhm et al. 1996). For the following computations we always use the currents determined from the Faraday cups because they are a better approximation to the true ion current than the electrical one.

The final step is to estimate the beam parameters on target. We assume that the measured electrical voltage according to Fig. 6 is always equal to the proton energy, while the product of the electrical voltage and the sum of the Faraday currents gives the total beam power P on the target at every time t. Taking the three single Faraday currents instead of the sum gives the beam power at the three different radial positions, i.e. beam angles, respectively. Possible additional losses of the proton current on the way between the diode gap and the target are not taken into account.

In order to derive a power *density* on target, a two-dimensional, rotationally symmetric Gaussian beam profile of the form

$$p(r) = P\frac{1}{2\pi\sigma^2}\exp\left(-\frac{r^2}{2\sigma^2}\right) \quad , \tag{15}$$

with a time independent full width at half maximum fwhm = 8 mm is assumed. For completeness we give here the relation between σ and the fwhm:

$$\sigma = \frac{\mathrm{fwhm}}{2\sqrt{(\ln 4)}} \quad . \tag{16}$$

The resultant power densities on target for the single Faraday currents as well as for their sum are given in Fig. 7.

With the power densities shown in Fig. 7 we performed the following simulations: Three computations with the power density according to the sum of the Faraday currents and at angles of incidence of 30°, 36° and 42° (single-beam computations), and a multiple-beam computation with three beams

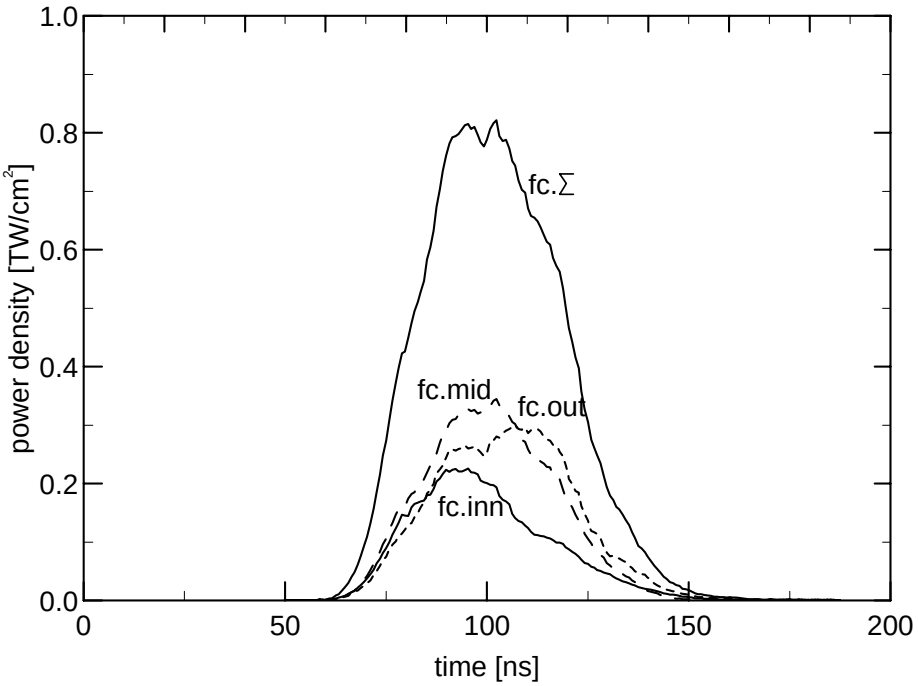

Figure 7: Power density of the B_{appl}-diode on target as derived from the three single Faraday currents (see text) as well as for their sum. For the beam profile, a 2D-Gaussian with a time independent fwhm of 8 mm has been assumed.

according to the inner, middle and outer Faraday current, entering the target and angles of 32°, 36° and 40° simultaneously.

The results of the computations are summarized in Fig. 8 in terms of the target back surface velocity. As for the B_Θ-diode, the single-beam computations at $\theta = 30°$ and 42° represent the most extreme assumptions that the full **KALIF** beam comes from one of these directions, and present the maximum and minimum achievable target velocities. And, although the three beam power densities in the multiple-beam computation come from different directions *and* differ in time, the resultant velocity is scarcely different from the single-beam computation with $\theta = 36°$. Thus, as for the B_Θ-diode, in the case of the B_{appl}-diode the simulations may be performed for single beams coming from a geometrically centered beam angle.

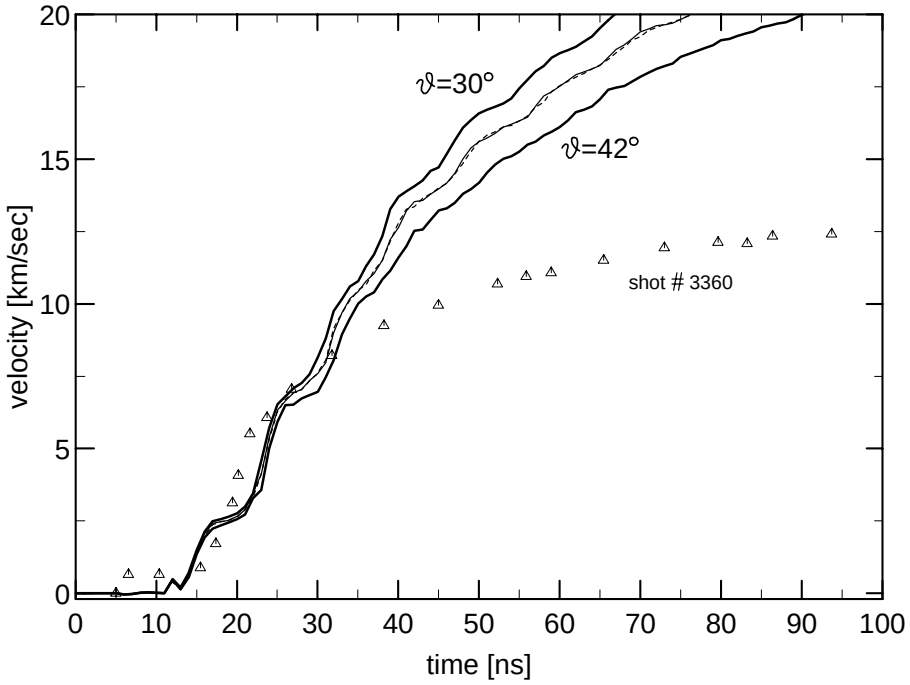

Figure 8: Simulated back surface velocities of a 50 μm thick aluminum after impact of the B_{appl} proton beam at different angles of incidence θ. Thick lines show calculations for single beams and $\theta = 30^\circ$ and 42°. The thin solid line shows a simulation with $\theta = 36^\circ$, the dashed line is a simulation for a non-homogeneous beam angle distribution (see text).

4 The effect of a proton beam energy distribution

The proton beam energy distribution of both, the B_Θ- and the $B_{\rm appl}$-diode has recently been measured with a magnetic energy analyzer (Bluhm et al. 1996). It was found that the width of the energy distribution is typically between 10 and 20% of the mean energy. Bluhm et al. also demonstrate that certain differences appear between the electrically measured voltage pulse shape and the ion energy behaviour. Namely, in the case of the B_Θ-diode the electrical voltage curve seems to well represent the average ion energy distribution measured with the magnetic energy analyzer at least during the voltage rise of a pulse for ion energies larger than 0.8 MeV. During the voltage decrease after the power density maximum the electrical signals seem to underestimate the average ion energy distribution. In the case of the $B_{\rm appl}$-diode no information is available from the magnetic energy analyzer for ion energies below about 1.2 MeV during the rise of the pulse, and even above this value the electrical voltage overestimates the average ion energies by about 10 %. These discrepancies between the electrical voltage signal and the average measured ion energies are not taken into account in this study. However, a more detailed discussion about these effects is included in section 9.

In order to define a proton energy distribution we start from a Gaussian

$$g(E,t) = \frac{1}{\sigma\sqrt{(2\pi)}} \exp\left(-\frac{(E-E_0)^2}{2\sigma^2}\right) \quad , \tag{17}$$

where $E_0(t)$ is the proton energy at time t according to Fig. 2,

$$\sigma(t) = \frac{\rm fwhm}{2\sqrt{(\ln 4)}} \quad , \tag{18}$$

and the full width at half maximum according to the measurements cited above is fwhm $= 0.2 \cdot E_0$, thus becoming time dependent. In this form, $g(E,t)$ is normalized at each time step, i.e.

$$\int_{-\infty}^{\infty} g(E)\, dE = 1 \quad , \tag{19}$$

and represents a distribution function of particles with respect to the proton energy, i.e., $g(E)\, dE$ is the fraction of the total number of particles found in the energy interval $[E, E+dE]$. Thus, taking $i(t)$ as the total current density of the beam at time t according to Fig. 2, the function $g(E)i(t)\, dE$ is the fraction of the total current density carried by particles in the energy intervall $[E, E+dE]$ at every time t, and $g(E)iE\, dE$ is their respective power density, since

$$\int_{-\infty}^{\infty} g(E,t)i(t)E(t)\, dE = P_{\rm tot}(t) \quad . \tag{20}$$

In order to simulate an energy distribution of the proton beam, at every time step we divided the function $g(E,t)$ of Eq. (17) into 9 equidistant energy intervalls between $E_0 \pm 3\sigma$, thus creating nine beams with individual energies $E_k(t)$ and power densities

$$P_k(t) = \int_{E_k-\frac{1}{3}\sigma}^{E_k+\frac{1}{3}\sigma} g(E,t)i(t)E_k(t)\, dE \quad . \tag{21}$$

In the simulations all these beams enter the target simultaneously at an angle of $\theta = 30°$.

The results of these calculations are compared in Fig. 9 with a single-beam computation for $\theta = 30°$ and a 75 μm thick aluminum foil. From this figure it becomes obvious that an energy distribution of

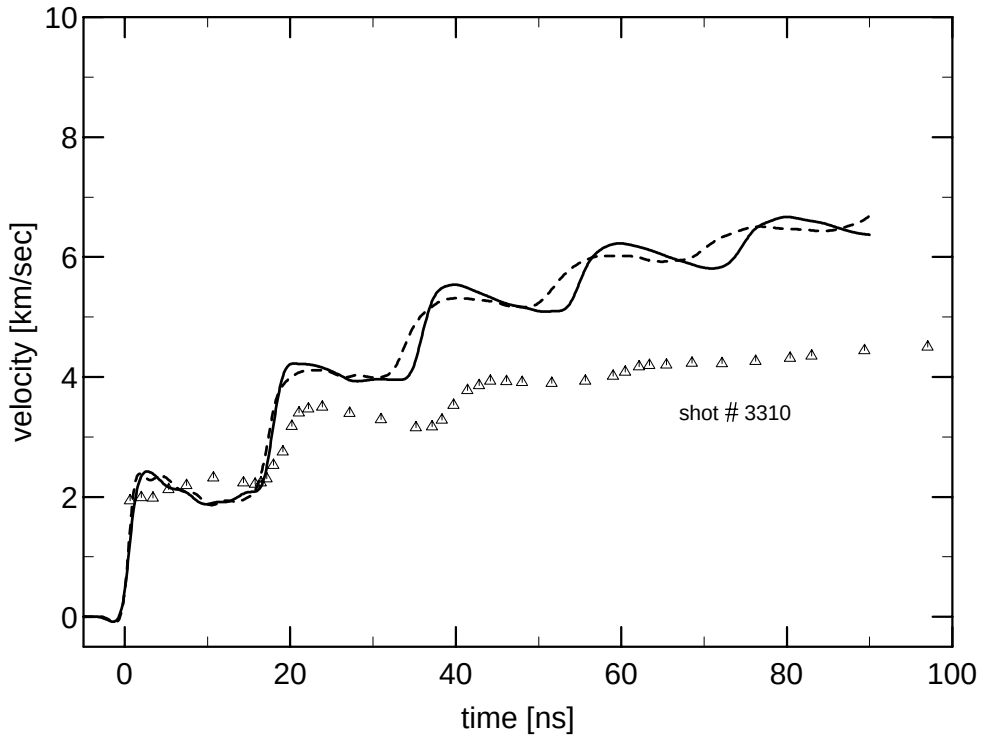

Figure 9: Simulated back surface velocities of a 75 μm thick aluminum foil after impact of the B_Θ-beam with and without energy distribution of the protons (see text). The angle of incidence in both cases is 30°.

protons smoothens the velocity steps due to different ranges of the interacting protons, and this smoothing is even larger than due to a beam angle distribution. We conclude that the proton energy distribution is one of the main reasons for the disappearence of the velocity steps in the measured data at late stages of evolution.

5 The influence of the maximum beam power density (B_Θ and B_{appl})

The shot to shot reproducibility of the proton beams produced by the **KALIF**-diodes is mainly influenced by the time jitter introduced by the self-breakdown water switches of the **KALIF** generator itself and by the problems related to the anode plasma generation. The maximum power density for regular shots varies from 0.1 to 0.2 TW/cm^2 for the B_Θ-diode and from 0.5 to 1 TW/cm^2 for the B_{appl}-diode. Unfortunately the analysis of the electrical signals measured close to the diode are of limited value only in order to reduce these uncertainties. In the computations we take into account the variation of the beam power density by increasing or decreasing the current density on target respectively while keeping the beam energy constant. Figures 10–13 show the respective computed back surface velocities as a function of time. The angle of incidence is $\theta = 30^\circ$ for the B_Θ and 36° for the B_{appl}-diode. Also shown in these Figures are measurements from individual experiments.

From these simulations it becomes obvious that it is impossible to fit all experiments by only an averaged beam profile even when changing the maximum available power density. For example, the simulation for B_Θ, 50 μm Al with $P_{max} = 0.15$ TW/cm^2 (Fig. 11) fits the experimental data quite well, especially the initial velocity jump. On the other hand, a simulation of a 75 μm foil with the same beam parameters (Fig. 12) does not give a correct behaviour of the initial velocity jump and the model overestimates the velocity during later phases. Decreasing the maximum power density may lead to an improvement in the later phase while a description of the initial velocity jump becomes even worse.

The situation becomes even more dramatic in the case of the B_{appl}-diode. The experimental data show a small velocity step starting at about 5 ns which cannot be reproduced by any of the models using the average beam profile of Figs. 6 and 7, and the target velocities become much too large at late stages of evolution. When the current density is scaled to achieve smaller peak power densities the final target velocity becomes smaller while the shape of the velocity curves as compared to the measurements cannot be improved. This result will be taken up once more in section 7.

These computations as well as the measured velocity data confirm that not only the maximum beam power but also the beam rise changes from shot to shot. Especially the beam rise up to the maximum proton energy is of crucial importance for an interpretation of the measured data (see also Baumung et al. 1994). Later on, most of the beam energy is deposited in the plasma and becomes only of minor importance for the target dynamics (see also section 7). Future measurements *must* have the task to measure the beam parameters on target, especially during the initial beam rise, so that computations can be performed with individual beam data for each shot.

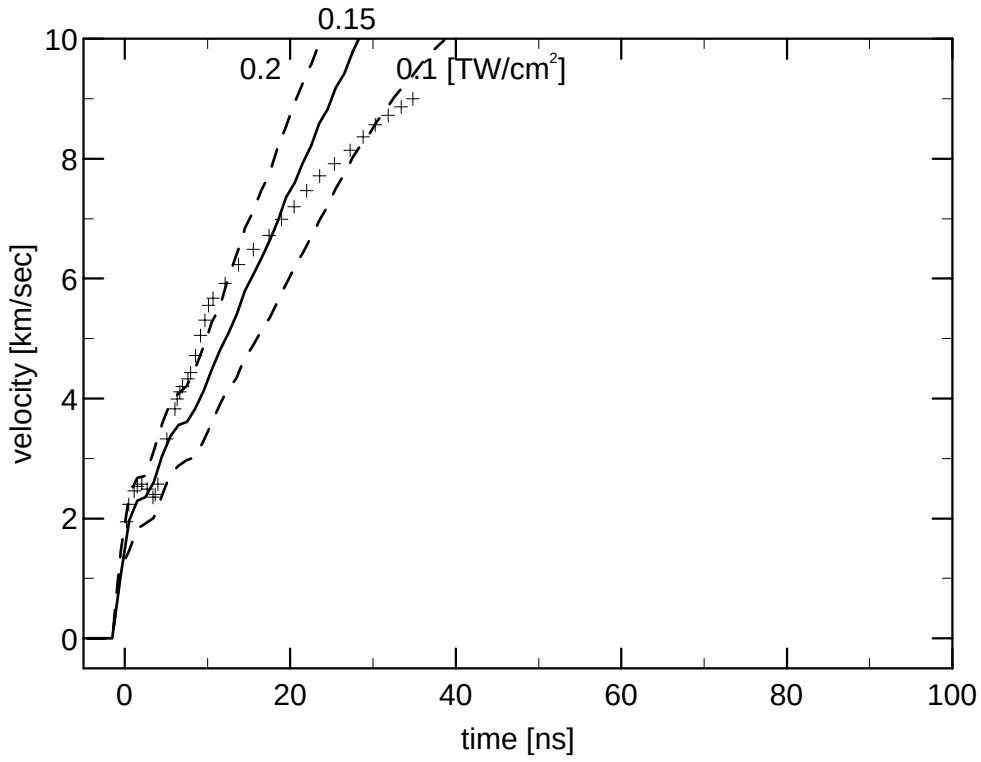

Figure 10: Simulated back surface velocities of a 33 μm thick aluminum target after interactions of B_Θ-beams with different maximum power densities. The crosses show experimental data of shot #3297.

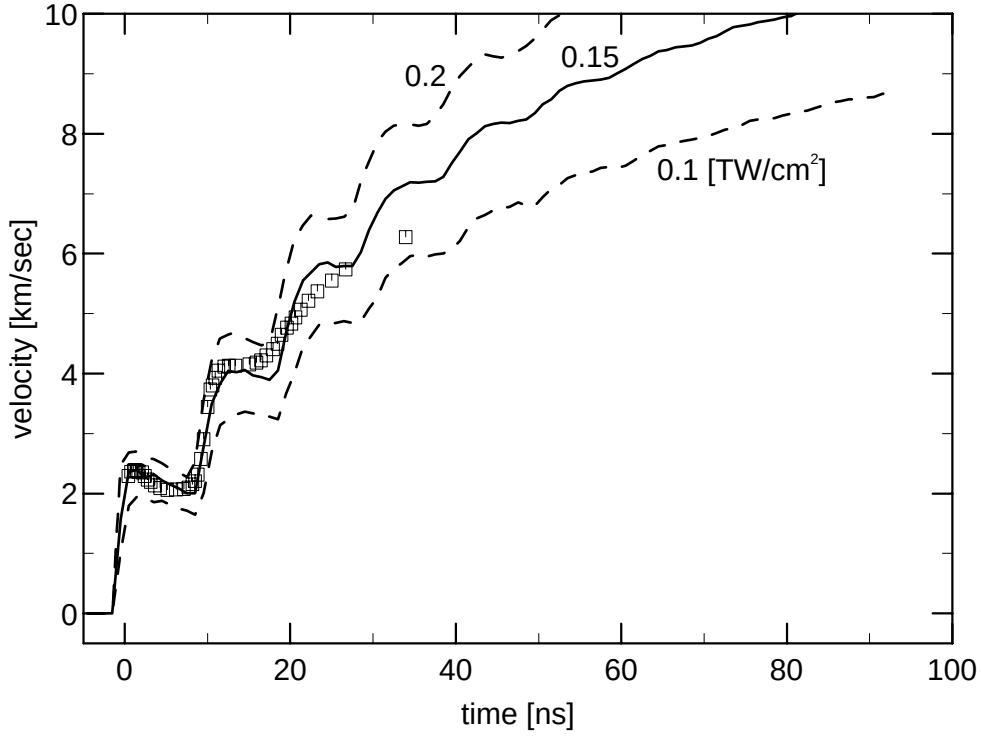

Figure 11: Simulated back surface velocities of a 50 μm thick aluminum target after interactions of B_Θ-beams with different maximum power densities. The squares show experimental data of shot #3332.

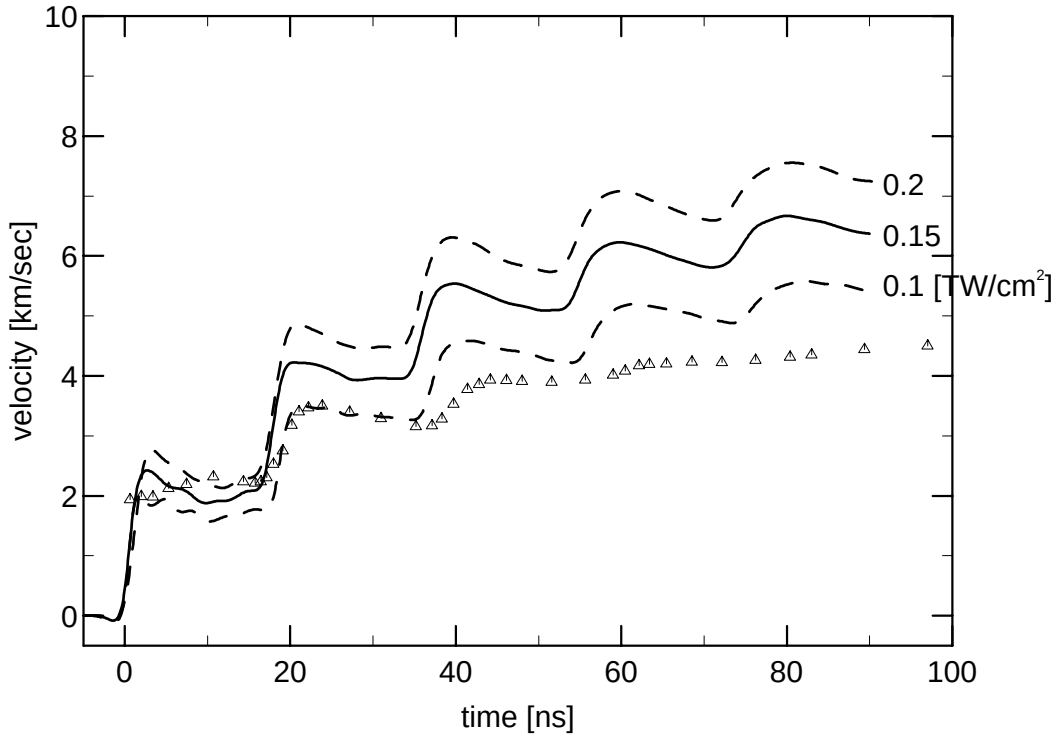

Figure 12: Simulated back surface velocities of a 75 μm thick aluminum target after interactions of B_Θ-beams with different maximum power densities. The triangles show experimental data of shot #3310.

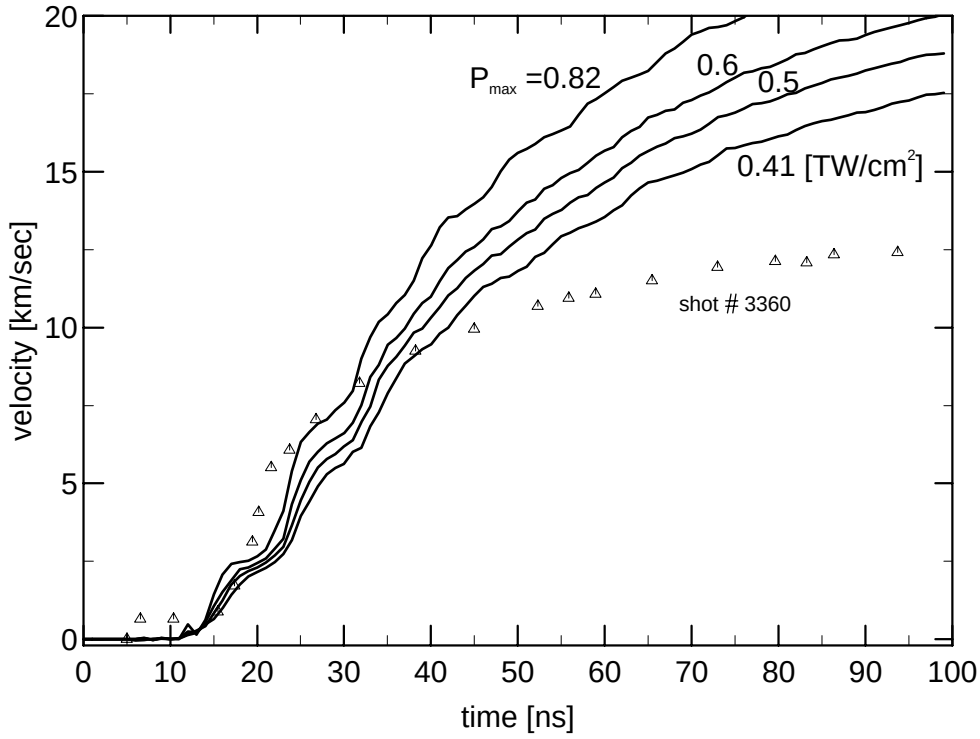

Figure 13: Simulated back surface velocities of a 50 μm thick aluminum target after interactions of B_{appl}-beams with different maximum power densities.

6 The influence of Bremsstrahlung and radiation transfer (B_Θ and B_{appl})

In this section we examine the role of radiation losses in **KALIF** beam-target experiments. Fig. 14 shows the result of simulations for B_Θ (75 μm Al, $P_{\max} = 0.15\,\mathrm{TW/cm^2}$, $\theta = 30^\circ$) without taking into account radiation, with 100 groups (i.e. frequency intervals) radiation transfer in diffusion approximation, and with pure Bremsstrahlung as a local loss without reabsorbtion. The computation of pure Bremsstrahlung only serves as a model sequence for comparison. Taking into account Bremsstrahlung as a local energy sink can be regarded as a simulation of a *completely* optically thin plasma, i.e. the locally produced diffuse radiation is *assumed* to be radiated without any interaction with neighbouring mass elements ($J = J(r,t)$ and $E_\mathrm{r} = 0$ in eq. (3)). In contrast, the no-radiation case represents $J = 0$ and $E_\mathrm{r} = 0$ in eq. (3), and for the 100 groups radiative transfer E_r is computed by solving the transfer equations (10)–(14) while $J = 0$.

According to Fig. 15 the maximum as well as the mass averaged temperature[2] of the model with pure Bremsstrahlung start to deviate significantly from the no-radiation case already at about 8 ns. As a result, the plasma pressure decreases leading to less acceleration of the remaining solid foil from about 10 ns (Fig. 14). A comparison with the case of 100 groups radiative transfer shows that the plasma is definitely not optically thin: The maximum and mass averaged temperatures of cases with and without radiative transfer only start to differ at about 60 ns, and the effect on the dynamics of the foil is negligible.

The corresponding spatial temperature profiles of model sequences with and without radiative transfer are shown in Figs. 16 and 17. The maximum temperature is always found at the Bragg peak of the energy deposition and is moving from the plasma-solid interface into the plasma after about the proton energy maximum (at about 30 ns for B_Θ). The temperature profiles become significantly different only after sufficient dilution of the expanding plasma.

Corresponding models for the B_{appl}-diode are shown in Figs. 18–21 (here we did not consider the case of pure optically thin Bremsstrahlung). In the case of the B_{appl}-diode the temperatures with and without radiative transfer start to differ already at about 35 ns because of a faster dilution of the plasma due to higher temperatures and corresponding pressures. Also, radiation losses are larger than in models for the less powerful B_Θ-diode. Furthermore, at higher temperatures the emission maximum of the radiation is shifted towards larger photon energies, where the absorption coefficients become smaller, and the radiation energy increases ($\propto T^4$). This leads to a larger penetration depth of radiation into the remaining solid thus increasing the speed of the ablation front. The penetration of radiation into the solid material is clearly seen as a moving temperature front at the plasma-solid interface in Figs. 20 and 21. The additional pressure generated by the moving ablation front in combination with the thereby reduced mass of the remaining solid leads to slightly larger expansion velocities during later phases of evolution (Fig. 18).

[2] At every time t we define the mass averaged temperature of the plasma by

$$\overline{T} = \frac{\sum T_k \, dm_k}{\sum dm_k}, \tag{22}$$

where the sumation is carried out over all mass elements k with temperatures above the evaporation temperature (2714 K for Al at normal pressure).

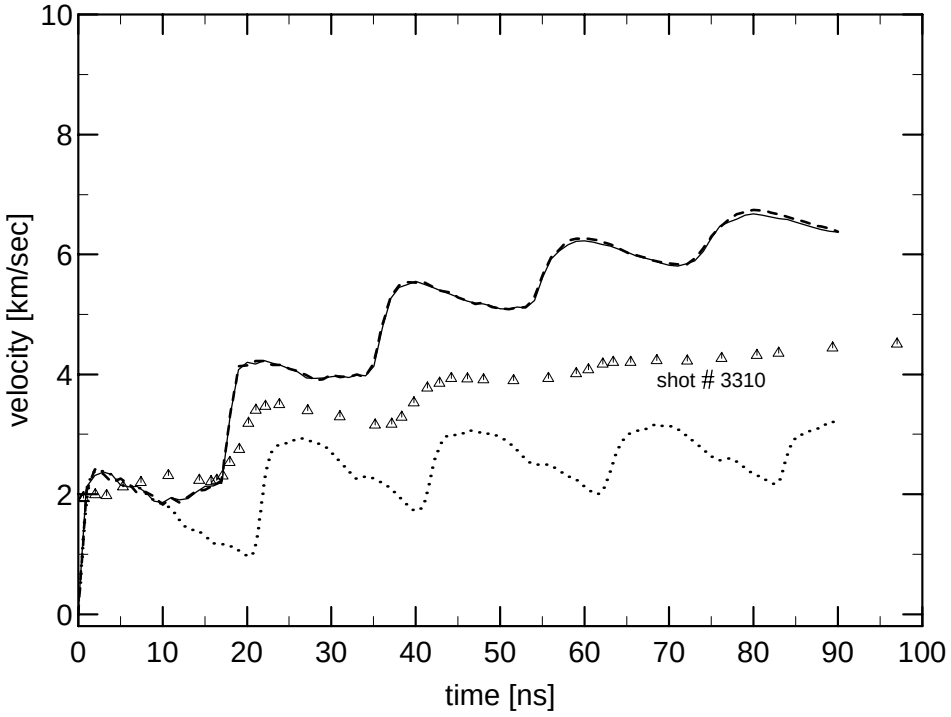

Figure 14: Simulated back surface velocities of a 75 μm thick aluminum target after impact of the B_Θ-beam without taking into account radiative transfer (solid line), with 100 groups radiative transfer (dashed), and with completely optically thin Bremsstrahlung (dotted, see text).

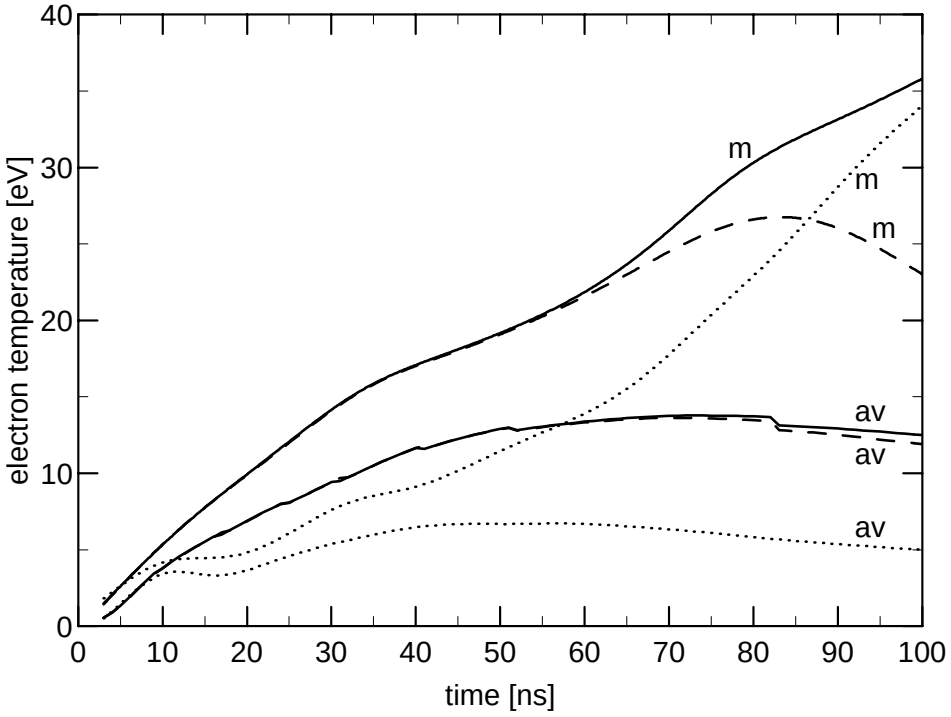

Figure 15: Maximum (m) and mass averaged (av) plasma temperatures for the models of Fig. 14 without (solid lines), with radiative transfer (dashed), and for completely optically thin Bremsstrahlung (dotted).

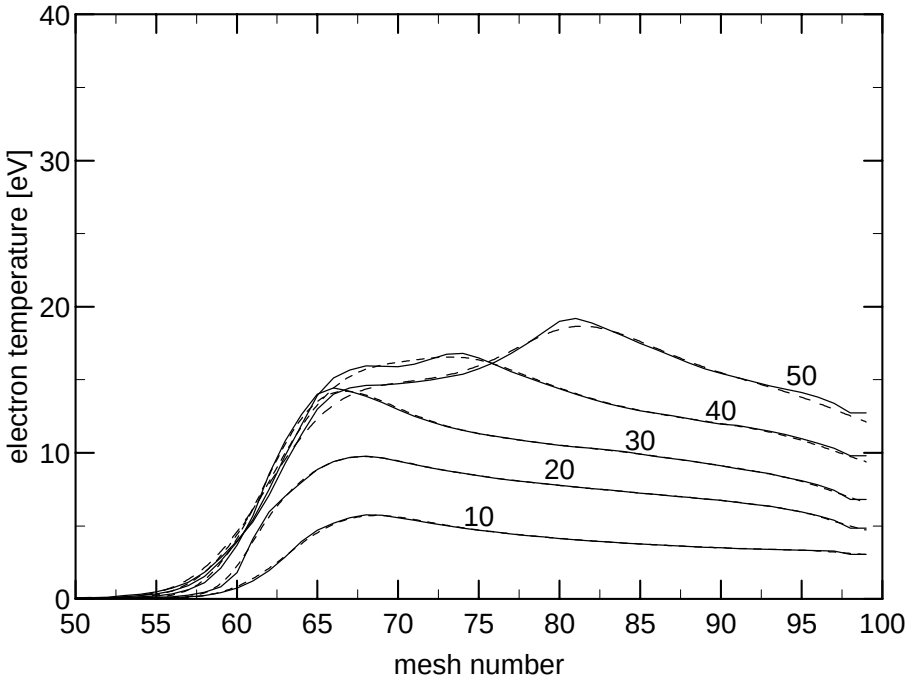

Figure 16: Temperature profiles as a function of the mesh number of models without (solid lines) and with radiative transfer (dashed). The B_Θ-beam comes from the right, time marks are given in [ns]. Note that the mesh cells do not all contain equal masses due to a non-equidistant spatial resolution of the initial model at $t = 0$!

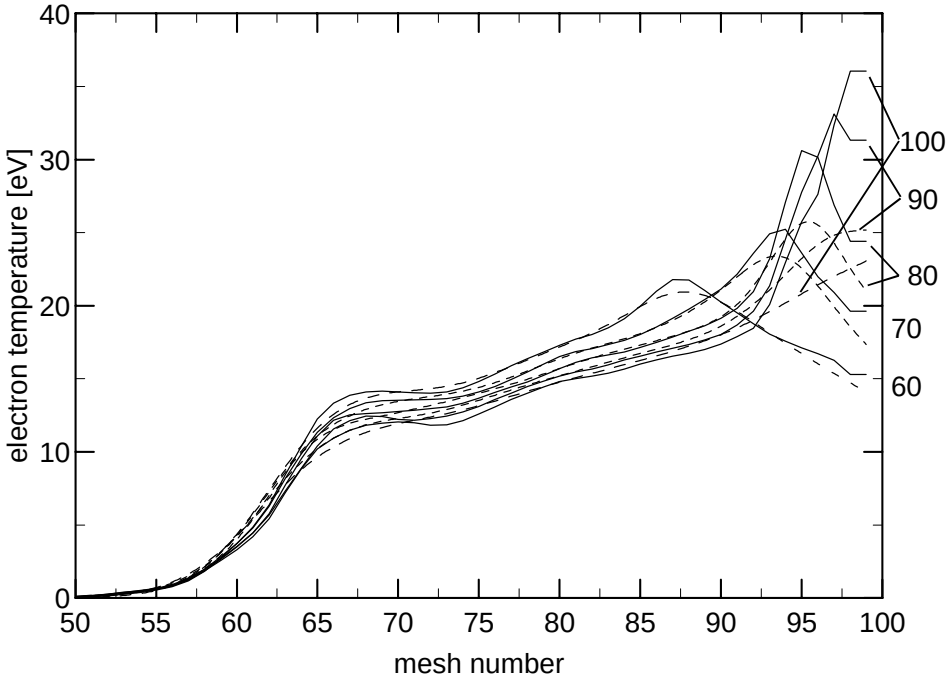

Figure 17: Temperature profiles as a function of the mesh number of models without (solid lines) and with radiative transfer (dashed). The B_Θ-beam comes from the right, time marks are given in [ns]. Note that the mesh cells do not all contain equal masses due to a non-equidistant spatial resolution of the initial model at $t = 0$!

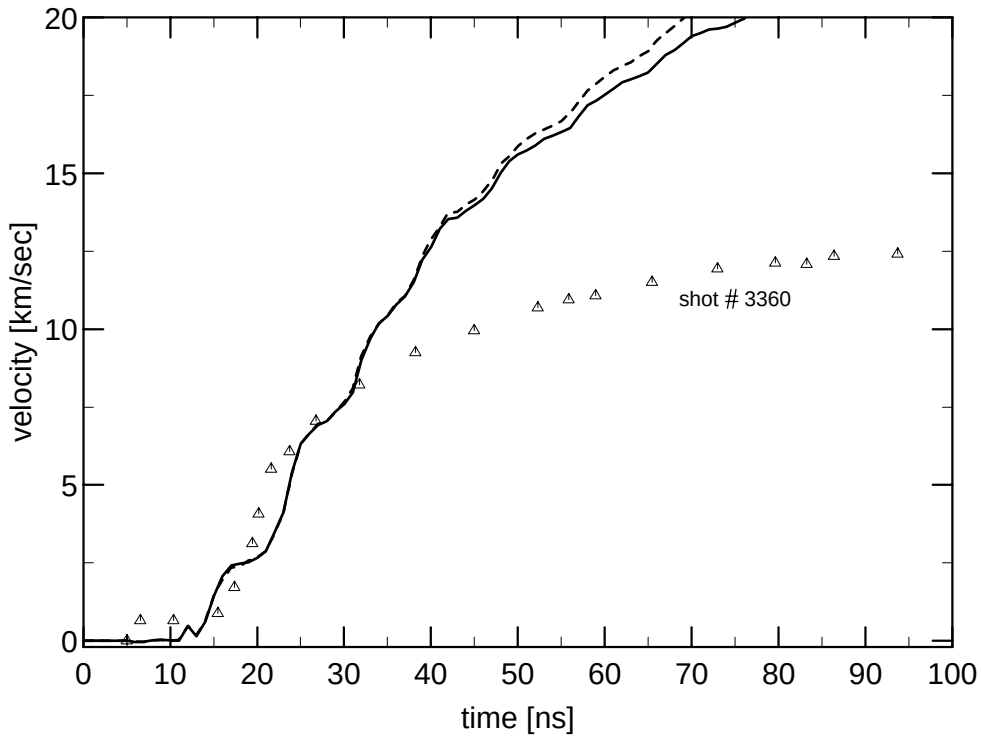

Figure 18: Simulated back surface velocities of a 50 μm thick aluminum target after impact of the B_{appl}-beam without taking into account radiative transfer (solid line) and with 100 groups radiative transfer (dashed).

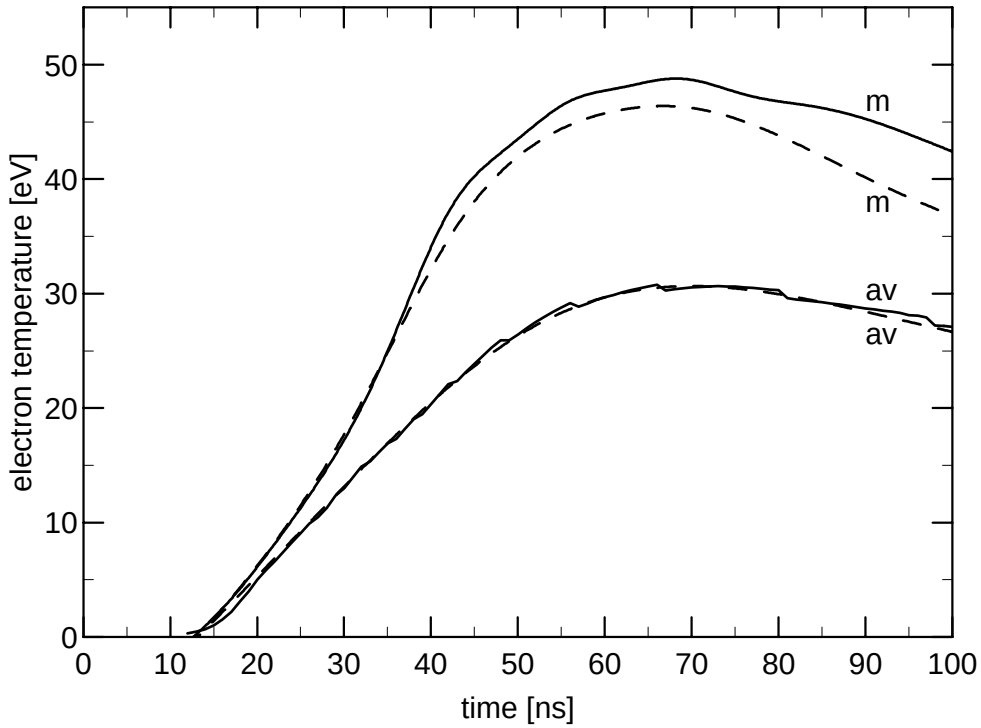

Figure 19: Maximum (m) and mass averaged (av) plasma temperatures for the models of Fig. 18 without (solid lines) and with radiative transfer (dashed).

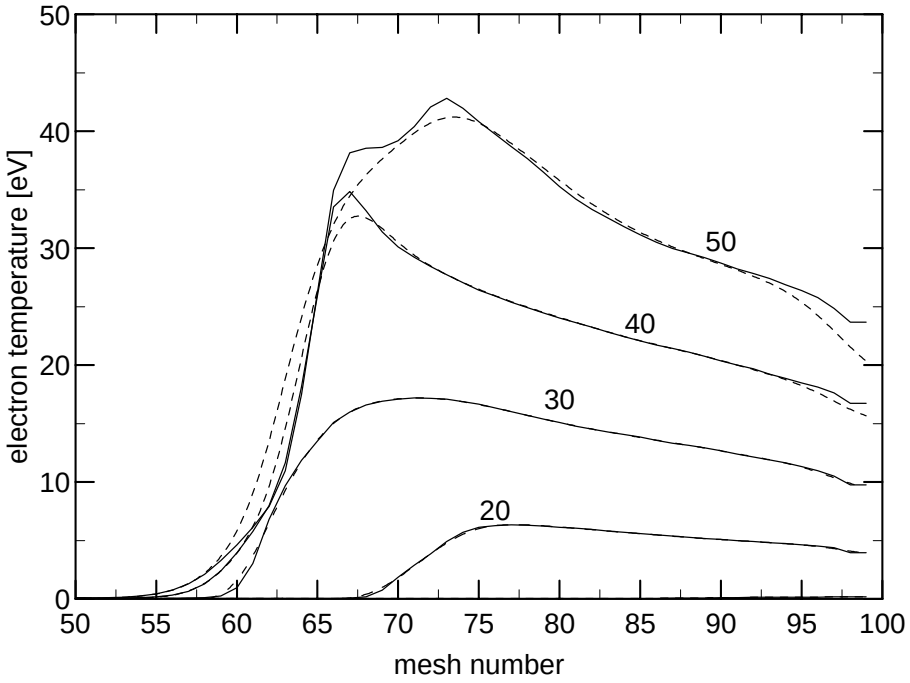

Figure 20: Temperature profiles as a function of the mesh number of models without (solid lines) and with radiative transfer (dashed). The B_{appl}-beam comes from the right, time marks are given in [ns]. Note that the mesh cells do not all contain equal masses due to a non-equidistant spatial resolution of the initial model at $t = 0$!

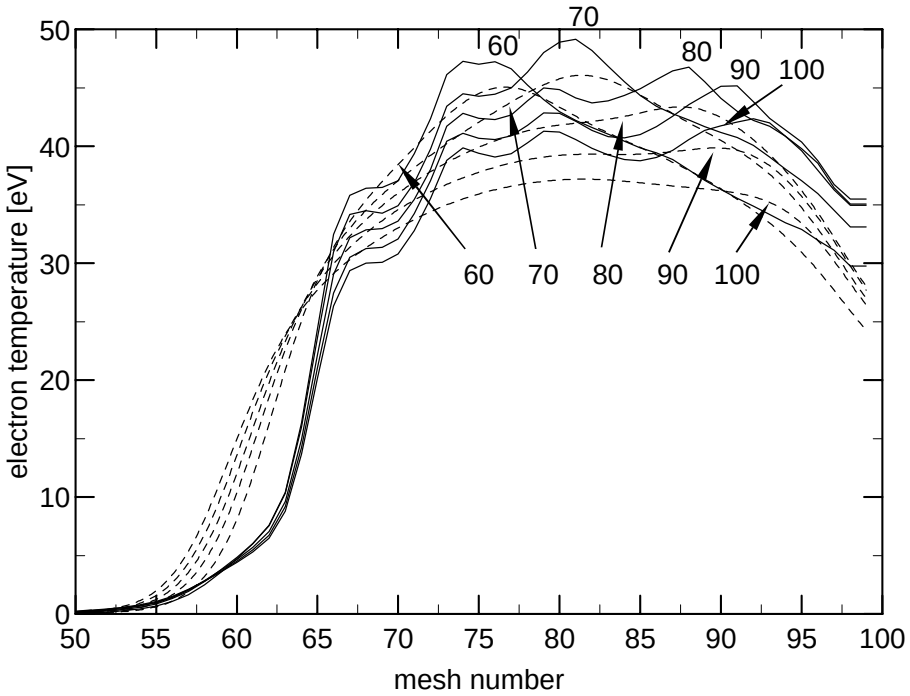

Figure 21: Temperature profiles as a function of the mesh number of models without (solid lines) and with radiative transfer (dashed). The B_{appl}-beam comes from the right, time marks are given in [ns]. Note that the mesh cells do not all contain equal masses due to a non-equidistant spatial resolution of the initial model at $t = 0$!

7 The influence of the beam rising- and decreasing time (B_{appl})

Simple estimates of the time-of-flight of protons with a given energy lead to the conclusion that the beam must be compressed (sometimes called beam bunching) during the voltage rise of the diode: Protons starting later in time with a higher kinetic energy may arrive at the target simultaneously with protons that have been emitted earlier with lower kinetic energy. Similar estimates lead to the conclusion that the beam is expanded during the voltage decrease after the diode voltage maximum. The simultaneous arrival of protons with different energies during the beam rise result in a small increase of the volumetric energy deposition upstream of the Bragg peak and a smearing of the Bragg peak itself. However, the current density of the B_{appl}-diode during the voltage rise according to Fig. 6 is so small that simulations taking into account a time-of-flight correction did not differ significantly from the already presented models and are therefore not shown here. To demonstrate the general effect of a sudden voltage rise we included in this section two computations where the beam has artificially been switched on at a given diode voltage (i.e. proton energy).

From Farady cup measurements it is known that in the case of the B_{appl}-diode at a certain moment near the diode voltage maximum a so-called parasitic load develops which leads to a rapid decrease of the proton current as compared to the electrical current signal (Fig. 6). In order to check the general consequences of such events, we performed two simulations where the beam is completely switched off soon *after* the diode voltage maximum as well as simulations where the beam is switched off already *before* the voltage maximum.

In detail, the parameters of the simulations presented in this section are:

- a sudden switch-on of the beam as soon as the proton energy E_p becomes $E_p > 1\,\mathrm{MeV}$ and $E_p > 1.2\,\mathrm{MeV}$, indicated by the left arrows in the beam parameter history of Fig. 22
- a sudden switch-off of the beam as soon as $E_p < 1.4\,\mathrm{MeV}$ and $E_p < 1.5\,\mathrm{MeV}$ *after* the diode voltage maximum, indicated by the two right arrows in the beam parameter history of Fig. 22
- a sudden switch-off of the beam *before* the diode voltage maximum, where the time of the switch-off, t_{off}, the corresponding proton energy and peak power density are given in in the following table:

Table 1:

model	t_{off} [ns]	E_p [MeV]	P [TW/cm^2]
1	89.84	1.60	0.76
2	88.28	1.57	0.70
3	85.94	1.52	0.60
4	82.03	1.47	0.49

The beam power maximum of the full **KALIF** B_{appl}-beam is at $t = 95.31\,\mathrm{ns}$, has a proton energy of $E_p = 1.54\,\mathrm{MeV}$ and a power density of $P = 0.82\,\mathrm{TW/cm^2}$.

The consequences for the target dynamics of an artificial switch-on of the beam are demonstrated in Fig. 23. With increasing strength of the initial pulse the first pressure wave generated in the solid part of the foil becomes stronger which manifests in more pronounced velocity steps. Again, these simulations demonstate the importance of the initial rise of the beam. Compared to the beam used in the simulations, the beam in shot #3360 must have had an even smoother initial rise with a prepulse.

The consequences for a sudden switch-off of the beam *after* the beam power maximum on the target velocity and temperature are shown in Figs. 24 and 25, respectively. The changes of the target velocity

are only small since the target acceleration takes place during the early phases of evolution, and the energy deposition zone decouples from the solid target with decreasing proton energies. However, the maximum as well as the mass averaged temperature immediately start to decrease significantly as soon as the beam is switched off. Obviously, these calculations demonstrate that the early phase of the beam can be studied by measuring the target velocity while the late phase can only be examined by measuring the plasma temperatures. This demands for a simultaneous measurement of the velocity *as well as* of plasma temperatures, which is presently not available.

The consequences for a sudden switch-off of the beam *before* the beam power maximum on the target velocity are shown in Fig. 26. It is interesting to note, that, according to Table 1, the switching off before the beam power maximum presents just an alternative way of reducing the maximum beam power as compared to the simple downscaling in section 5. Obviously, this switch-off gives a much better fit to the measured velocity curve and is also consistent with our recent knowledge of the development of a parasitic load in the diode! For completeness we also give the maximum and mass averaged temperatures of these models in Fig. 27. However, these temperatures should only be used as a first estimate since the abrupt beam switch-off done in these simulations might be not very realistic. In reality, the beam current will decrease more slowly so that further energy is deposited in the plasma, thereby keeping the temperatures higher on average.

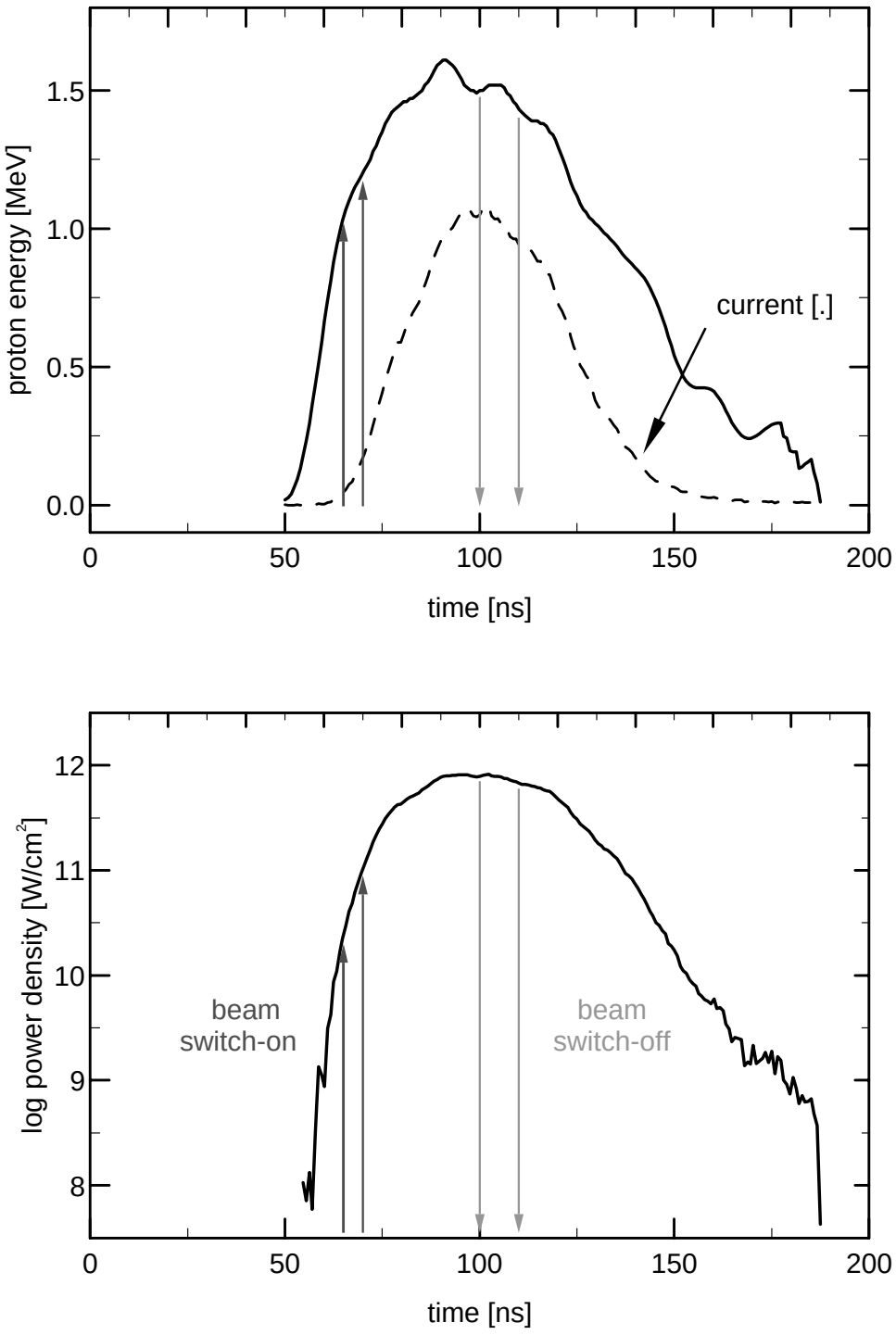

Figure 22: Voltage, current and power density as a function of time for the B_{appl}-diode. The arrows indicate the artificial switch-on at $E_p > 1\,\mathrm{MeV}$ and $E_p > 1.2\,\mathrm{MeV}$, and the artificial switch-off at $E_p < 1.4\,\mathrm{MeV}$ and $E_p < 1.5\,\mathrm{MeV}$ used in the calculations (see text).

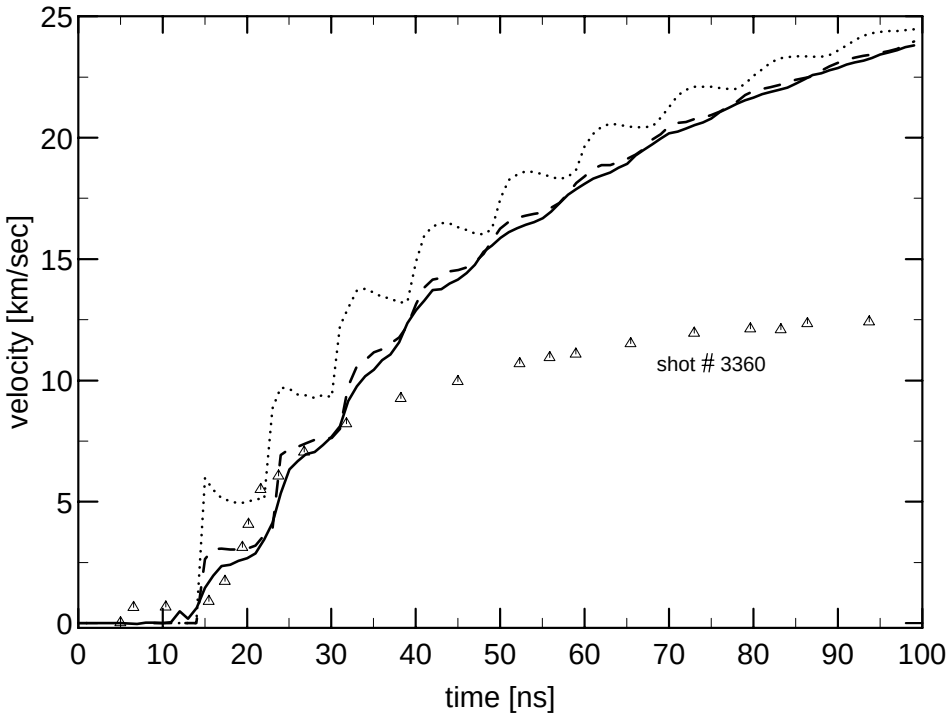

Figure 23: Simulated back surface velocities of a 50 μm thick aluminum target after impact of the B_{appl}-beam. Solid line: full **KALIF** beam; dashed: beam switched on at $E_p > 1$ MeV; dotted: beam switched on at $E_p > 1.2$ MeV.

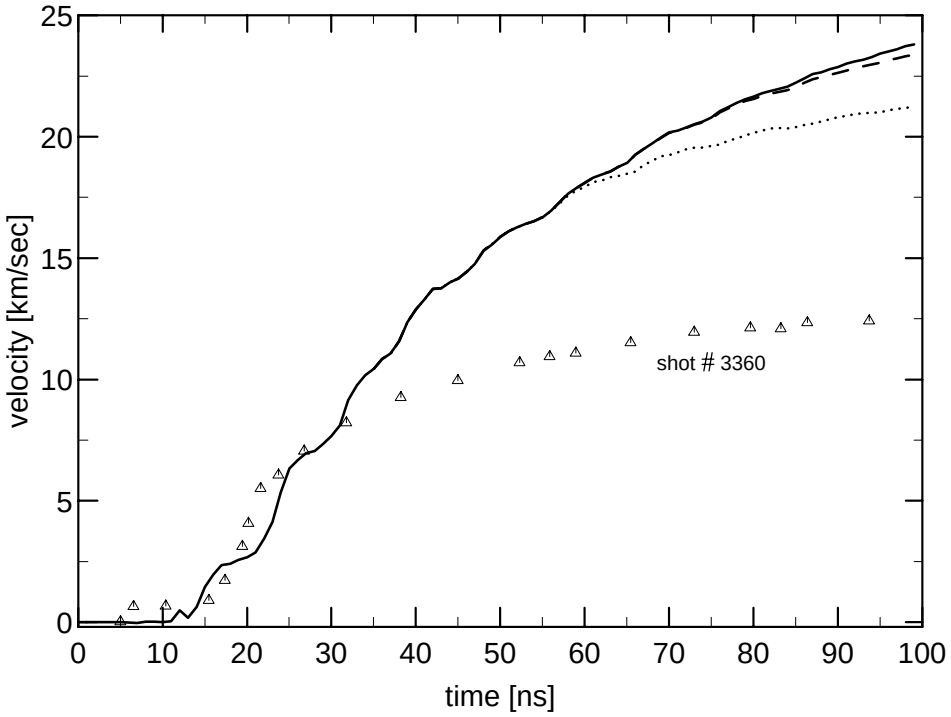

Figure 24: Simulated back surface velocities of a 50 μm thick aluminum target after impact of the B_{appl}-beam. Solid line: full **KALIF** beam; dashed: beam switched off at $E_p < 1.4$ MeV; dotted: beam switched off at $E_p < 1.5$ MeV *after* the diode voltage maximum.

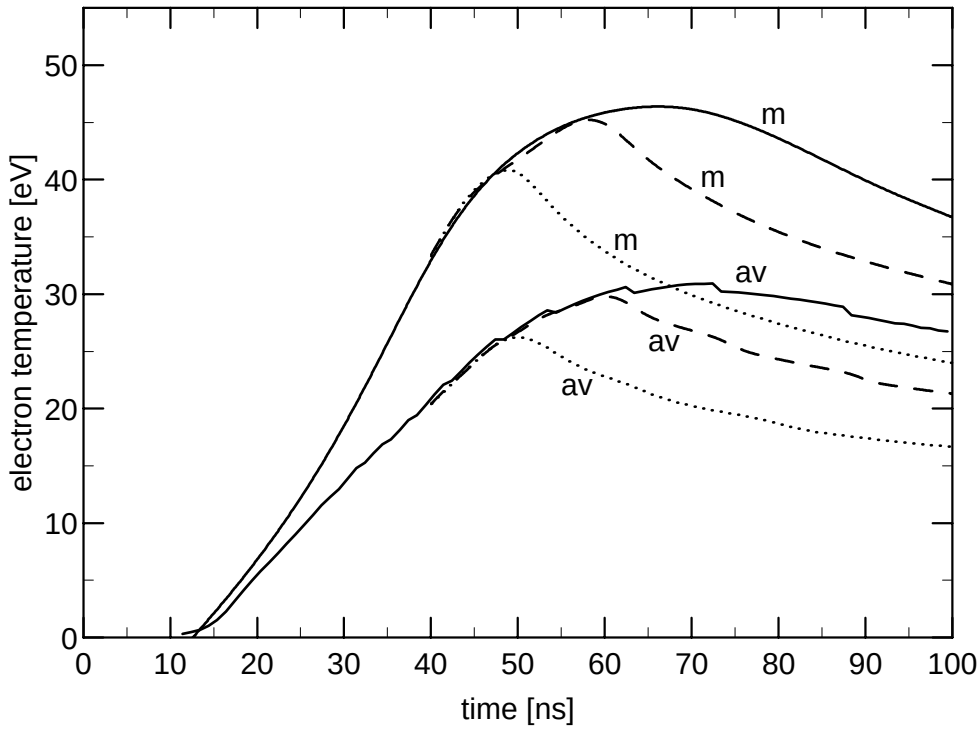

Figure 25: Maximum (m) and mass averaged (av) plasma temperatures of a 50 μm thick aluminum target after impact of the B_{appl}-beam. Solid line: full **KALIF** beam; dashed: beam switched off at $E_p < 1.4$ MeV; dotted: beam switched off at $E_p < 1.5$ MeV *after* the diode voltage maximum.

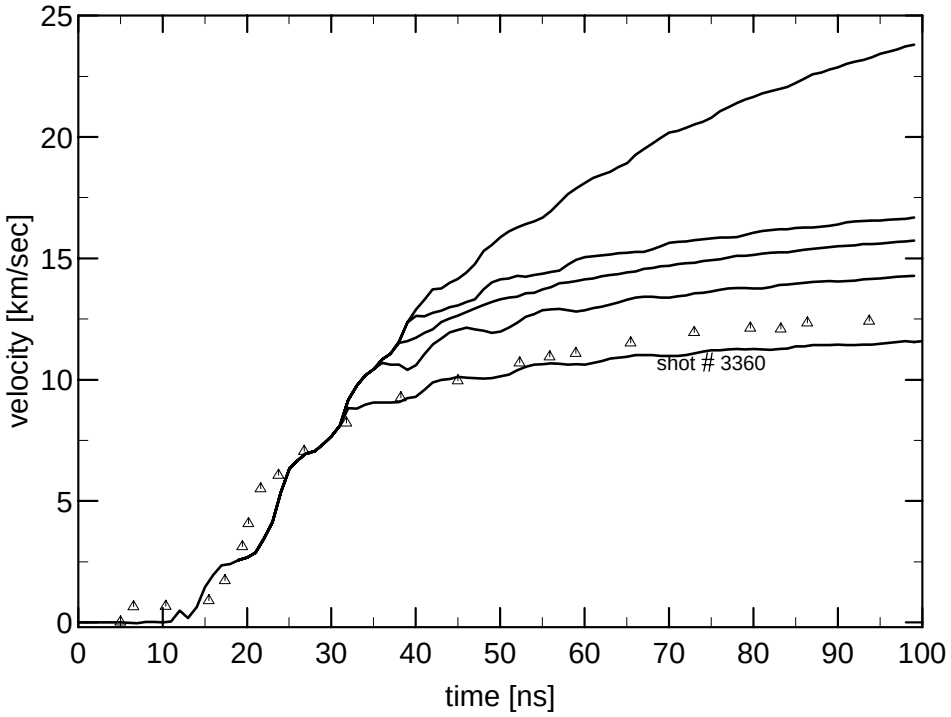

Figure 26: Simulated back surface velocities of a 50 μm thick aluminum target after impact of the B_{appl}-beam. From top to bottom: full **KALIF** beam, models 1–4 from table 1.

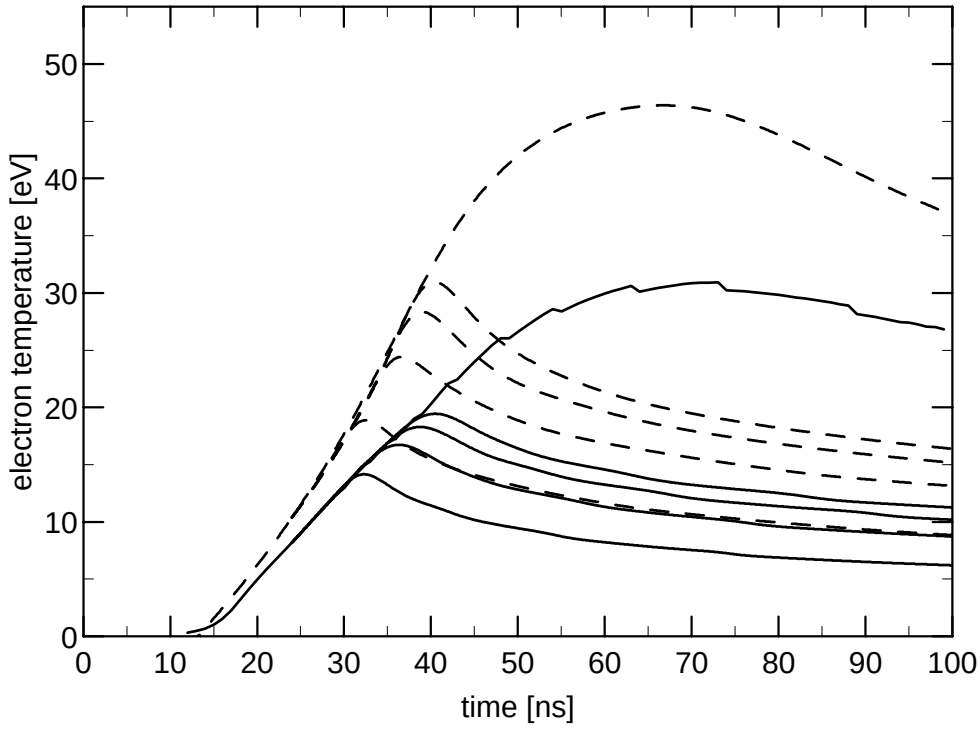

Figure 27: Maximum (dashed) and mass averaged (solid lines) plasma temperatures of a 50 μm thick aluminum target after impact of the B_{appl}-beam. From top to bottom these curves represent models for the full **KALIF** beam and models 1–4 from table 1.

8 Two dimensional simulations of beam-target interactions (B_Θ)

One dimensional simulations in slab geometry imply a spatially homogeneous beam power distribution on the target. On the other hand, the experimentally determined spatial beam is more like a two dimensional Gaussian with a flat top and, accordingly, the maximum acceleration of the targets has always been found in the beam center (Baumung et al. 1995). Here we study the consequences of a non-homogeneous beam power disribution on the target dynamics using a 2D Godunov-type hydrodynamic scheme on moving grids in cylindrical symmetry (Fortov at al. 1996).

Aluminum foils of 33 and 75 μm initial thickness are irradiated by the B_Θ proton beam of Fig. 2. The beam power distribution $P(r,t)$ on the target is assumed to be either homogeneous, i.e.

$$P(r,t) = P_0(t) \ , \tag{23}$$

or Gaussian shaped, i.e.

$$P(r,t) = P_0(t)\, exp(-r^2/2\sigma^2) \ , \tag{24}$$

where $P_0(t)$ is the B_Θ power density in the beam center at time t, r is the radial distance from the beam center and σ is the standard deviation for the experimentally determined full width at half maximum of 8 mm. The simulated targets always have a diameter of 1 cm.

Fig. 28 shows the computed back surface velocity of the flyer as a function of the radial position and time for the 33 μm foil. Computations of this kind can directly be compared to the space and time resolved measurements performed at **KALIF** (see e.g. Fig. 6b in Baumung et al. 1996). These velocities show small oscillations with time due to wave reverberations inside the solid part, which are induced by the first strong pressure pulse. Fig. 29 compares the computed back surface velocities as measured in the beam center for homogeneous and Gaussian beam profiles and initial target thicknesses of 33 and 75 μm. The wave reverberations in the 33 μm target are noticed as small oscillations while in the 75 μm target the first shock reflection at the back surface generates a large velocity jump at about 10 ns. Interestingly, the velocities in the center of homogeneous and Gaussian shaped beams agree quite well, indicating that pressure gradients tangential to the target surface can only be of minor importance for the target dynamics during the first few tens of nanoseconds. Quantitatively, this can be proven by comparing the spatial velocity distribution with the initial Gaussian of the power density. For example, the ratio of power densities from a 2D Gaussian at $r = 0$ and $r = \sigma$ is 0.606. After 20 ns the ratios of the computed back surface velocities at these radii are ≈ 0.59 for 33 μm and ≈ 0.67 for 75 μm Al. Due to the large ratio of the target diameter to target thickness (here of the order of 100-300) and due to the short measuring period (typically a few tens of nanoseconds in the experiments) radial disturbances do not evolve significantly. These results have two interesting consequences: 1) an approximate spatial power density distribution of the **KALIF** beam can directly be determined from the measured velocity distribution on the target back surface. 2) since neighbouring surface elements of the target expand almost independently of each other, the target dynamics can be studied by 1D simulations at different radial beam positions without a significant loss of accuracy.

It should be noted that any dissipation mechanism not included in these two dimensional computations (like e.g. thermal conduction or radiative transfer) may modify these results. Thermal conduction or radiative transfer may reduce the temperature and therefore the pressure in the beam center by transport of energy tangential to the target surface. On the other hand, the 1D calculations in this report and in Marten et al. (1996) have already shown that thermal conduction and radiative transfer are only second order effects for conditions valid at **KALIF**.

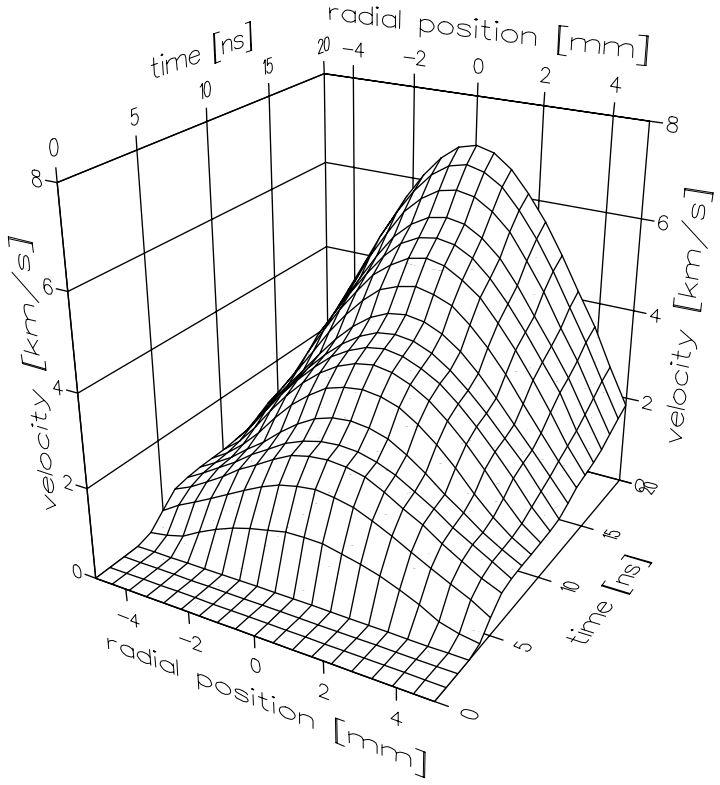

Figure 28: Computed back surface velocity as a function of radial position and time for a Gaussian beam profile. The target is a 33 μm Al foil.

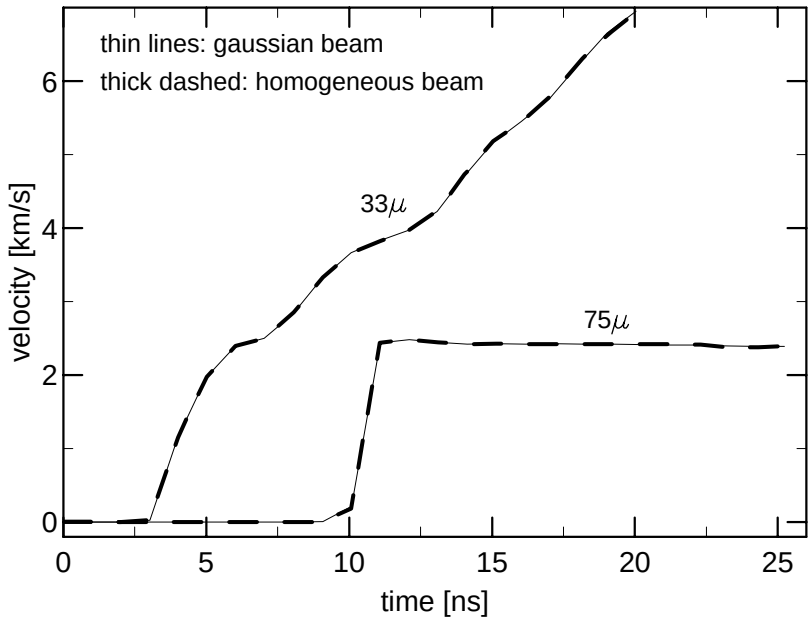

Figure 29: Computed back surface velocities in the beam center for spatially homogeneous and for Gaussian beam profiles for two different targets.

9 Discussion and Conclusions

This report presents a collection of numerical experiments which help to understand the influence and magnitude of different parameters and physical processes involved in beam-target interaction experiments performed at **KALIF**. Since we did not intend to find a "best fit" to experiments, not all of the investigated effects have been checked for both currently used **KALIF**-diodes (B_Θ and $B_{\rm appl}$), nor did we try to combine all of them.

We started this work by comparing different codes which are able to describe the proton-beam impact on aluminum foils under conditions valid at **KALIF**. It turned out that almost all of the studied effects produced differences which are larger than the differences of the results between the tested codes.

The beam-angle distribution of protons and the radial development of the diode current with time in the case of the $B_{\rm appl}$-diode are effects which follow either from the diode geometry or have been determined experimentally. The computations have demonstrated that such angular distributions of protons are only of minor importance for the target dynamics. In general, they result in a distribution of proton ranges leading to a weak smoothing of the measured back surface velocity without significant changes of the overall target acceleration. However, for both diodes (B_Θ and $B_{\rm appl}$) it is important to take into account the correct *average* angle where the protons come from.

A similar but larger effect on the measured target velocities is expected from an intrinsic proton beam energy distribution. The respective simulations performed for the $B_{\rm appl}$-diode where based on recent measurements with a magnetic energy analyzer. Likely, the proton energy distribution is one of the main reasons for the disappearance of the steps in the measured back surface velocity at late stages of target evolution.

A further effect of second order importance for the target dynamics is that of energy transport from the hot plasma into the cold solid material by radiation or thermal conduction. Both processes become more important with increasing plasma temperature (i.e. deposited energy), that is, they are more important in $B_{\rm appl}$-experiments. Radiation in general also decreases the temperature of the plasma. The computations have shown that the aluminum plasma is rather optically thick so that not much of its thermal energy is lost by radiation. Wether or not temperature changes of up to 10 % due to radiation could be resolved by emission spectroscopy has still to be demonstrated. A systematic study of theoretical K_α-spectra is just under development.

A detailed knowledge of the beam history **at the target** may be regarded as being of "first order importance" for understanding the target dynamics. Every modification of beam parameters done in this study resulted in a much larger change of the target dynamics or plasma temperatures than all of the previously discussed effects. The basic beam parameters entering the computations are the proton beam energy, and the proton current density or power density at the target, respectively. For the B_Θ-simulations the proton beam energy at the target was approximated by the diode voltage, averaged over about 10 shots, and time-of-flight corrected according to the distance of the target from the diode. The used proton power density at the target was approximated on the basis of electrical diode signals, again time-of-flight corrected *and* scaled with the peak proton power density from LiF/Cu activation measurements of $0.15\,\mathrm{TW/cm^2}$. In the computations, the proton power density has further been scaled within the experimental uncertainty of $0.15\pm0.05\,\mathrm{TW/cm^2}$. The agreement between the models and observations for the 50 μm Al target is remarkable, the observations for 33 μm Al are within the limits of the models, while the models do not show a correct behaviour with time, and for 75 μm Al the models predict too large velocities even for a beam with maximum beam power density of only $0.1\,\mathrm{TW/cm^2}$, although the lengths of the single velocity plateaus are about correct. These models demonstrate that due to the weak reproducibility of the diode operation it is not possible to perform satisfactory simulations of individual experiments only with average beam parameters.

For the $B_{\rm appl}$-simulations the proton beam energy at the target has been approximated by an average diode voltage, and the current density at the target has been derived from average Faraday currents measured in the diode gap. We think that these numerical simulations present **the key** for future models

and experiments: It has been shown that the observed back surface velocities can not be explained by simply downscaling the proton current densities. However, the models could significantly improved by cutting off the beam before the peak power of the electrical signals, which is consistent with the idea of the development of a parasitic load in the diode! Furthermore, switching off the beam at different times during the diode current rise results in drastical changes of the plasma temperature, which should be measurable. This demands for a simultaneous observation of velocities *and* temperatures (spectra) during indvidual shots, and should be a challenge for the future emission spectroscopy of K_α-satellites.

There is a further weak point common to all simulations performed in this study. Namely, the time history of beam parameters have been derived either from electrical signals of, or from ion beam measurements inside the diode, thereby assuming that no significant losses or changes (except for time-of-flight effects) take place between the diode and the target. Measurements of the ion energy distribution by means of a magnetic energy analyzer have shown that there is a discrepancy between the electrical voltage and the ion energies. This discrepancy seems to be not very large. However, an incorrect ion energy leads to an inaccurate specific energy deposition in the models which is the driving force for target accelerations. The situation seems to be much worse for the ion current. By LiF/Cu activation measurements it has been shown that the correlation between the electrical and the ion current is only weak, at least for the B_Θ-diode. There are three main possibilities to improve this situation:

- to improve the reproducibility of the ion beam
- to model the beam transport between the diode and the target
- and/or to *measure* the beam parameters at the target during each individual **KALIF** shot.

Finally, the two-dimensional simulations of the beam-target interaction are promising. They have demonstrated that a space and time resolved measurement of the target velocity may give information about the initial rise of the beam pulse, the achieved power density on the target *and* the spatial profile of the beam!

10 References

Baumung K., Bluhm H.-J., Goel B., Hoppé P., Karow H.U., Rusch D., Fortov V.E., Kanel G.I., Razorenov S.V., Utkin A.V., Vorobiev O.Yu., 1996, Laser and Particle Beams 14, 181

Baumung K., Karow H.U., Rusch D., Bluhm H.-J., Hoppé P., Kanel G.I., Utkin A.V., Licht V., 1994, J.Appl.Phys 75, 7633

Baumung K., Rusch D., Singer J., Razorenov S.V., Utkin A.V., Kanel G.I., 1995, Hydrodynamic Beam-Target Experiments on KALIF. In: H.-J. Bluhm (ed.) Physics of Intense Light Ion Beams and Production of High Energy Density in Matter, Annual Report 1994, Forschungszentrum Karlsruhe FZKA 5590, p. 73

Bluhm H.-J., Arzhannikov A., Buth L., Hoppé P., Licht V., Matveenko A., Rusch D., Stoltz O., Singer J., Singleton C., Tauschwitz A., Väth W., Yoo S., 1996, Ion diode diagnostics to resolve beam quality issues. In: H.-J. Bluhm (ed.) Physics of Intense Light Ion Beams, Production of High Energy Density in Matter, and Pulsed Power Applications, Annual Report 1995, Forschungszentrum Karlsruhe FZKA 5840, p. 35

Bushman A.V., Fortov V.E., Lomonosov I.V., 1989, Proc. Enrico Fermi School 1989, Elsevier Publ., p. 249

Fortov V.E., Goel B., Munz C.-D., Ni A.L., Shutov A.V., Vorobiev O.Yu., 1996, Nucl. Sci. Eng. 123, 169

Goel B., Höbel W., Würz H., 1993, Numerical Simulation of Radiation Transport on Supercomputers. In: H. Küsters (ed.) Proc. of the Joint Internat. Conf. on Mathematical Methods and Supercomputing in Nuclear Applications, Karlsruhe, April 19-23, 1993 Vol. 2, p. 63

Goel B., Vorobiev O.Yu., 1996, Laser and Particle Beams 14, 637

Gupta N.K., Goel B., Marten H., Höbel W., 1997a, Internal Report, Forschungszentrum Karlsruhe

Gupta N.K., Goel B., Marten H., Höbel W., 1997b, Internal Report, Forschungszentrum Karlsruhe

Hoppé P., Bachmann H., Bauer W., Bluhm H.-J., Buth L., Massier H., Rusch D., Stoltz O., Väth W., 1995, Characteristics of the Ion Beam Produced by the B_Θ Diode. In: H.-J. Bluhm (ed.) Physics of Intense Light Ion Beams and Production of High Energy Density in Matter, Annual Report 1994, Forschungszentrum Karlsruhe FZKA 5590, p. 51

Marten H., Goel B., Höbel W., 1996, Slowing down of an ablatively accelerated foil after impact on a stationary target. In: H.-J. Bluhm (ed.) Physics of Intense Light Ion Beams, Production of High Energy Density in Matter, and Pulsed Power Applications, Annual Report 1995, Forschungszentrum Karlsruhe FZKA 5840, p. 99